

Copyright  
by  
Himanshu Arora  
2011

The Thesis Committee for Himanshu Arora  
certifies that this is the approved version of the following thesis:

**The Influence of Earthquake Ground Motion on  
Wind Turbine Loads**

APPROVED BY

SUPERVISING COMMITTEE:

---

Lance Manuel, Supervisor

---

Loukas F. Kallivokas

**The Influence of Earthquake Ground Motion on  
Wind Turbine Loads**

by

**Himanshu Arora, B.Tech.**

**THESIS**

Presented to the Faculty of the Graduate School of  
The University of Texas at Austin  
in Partial Fulfillment  
of the Requirements  
for the Degree of

**Master of Science in Engineering**

THE UNIVERSITY OF TEXAS AT AUSTIN

May 2011

Dedicated to my family and friends

## Acknowledgments

I give my sincere thanks to my advisor, Dr. Lance Manuel, for providing me with the basis of knowledge necessary to undertake this project, and for the guidance necessary to finish it. His significant contribution of time and knowledge to this project is gratefully acknowledged. I thank, Dr. Loukas F. Kallivokas, for serving on this committee and giving thoughtful advise. I would like to convey my sincere gratitude to Dr. Ian Prowell, formerly, a doctoral student at the University of California-San Diego, for providing us with his wind turbine response simulation model for analysis of earthquake loading in FAST and for his continued assistance with the model. As well, I would like to thank Dr. Jason Jonkman of the National Renewable Energy Laboratory for his assistance with the FAST code. I would also like to thank my friend and fellow research group member, Abhinav Sultania, for helping me getting started with this research project and providing insightful inputs at its various stages.

I want to thank my parents, sister, and friends for their unconditional love and support. Last but not the least, want to express gratitude to God, for giving me the strength and patience to pursue all my endeavors.

# The Influence of Earthquake Ground Motion on Wind Turbine Loads

Himanshu Arora, M.S.E.

The University of Texas at Austin, 2011

Supervisor: Lance Manuel

The design of wind turbines installed in various regions of the world where earthquakes are likely must take into account loads imposed on the turbine due to ground shaking. Currently, design standards such as the International Electrotechnical Commission's standard, IEC 61400-1, do not provide detailed guidelines for assessing loads on wind turbines due to seismic input excitation. In regions of high seismic hazard, it is extremely important to perform a thorough seismic analysis. Various simplified and full-system wind turbine models have been published and used for seismic analysis of turbine loads in recent years. Among these models, the open-source software, FAST, allows for full-system simulation of the response of wind turbines subjected to earthquake ground motion along with other sources of loading such as from the mean wind field and turbulence. This study employs this open-source software to simulate seismic loads and presents statistical and spectral summaries resulting from extensive analyses undertaken by simulating turbine response to various input motions from Western U.S. earthquakes. A total of 150 different earthquake ground motion records with varying magnitude and distance

from fault rupture are selected and normalized/scaled to selected target levels prior to response simulation using a utility-scale 5-MW wind turbine model. The records selected are divided into six groups of 25 records each; the groups consist of different magnitude and distance-to-rupture values. The records in each bin are scaled to have similar demand levels as the average of the demand of the unscaled records in that bin. Two different normalization options are considered—in one, the scaling is at the rotor rotation rate (or the once-per-rev or 1P frequency) ; in the other, the scaling is done at the tower fore-aft first mode frequency. A study of various turbine load measures is conducted. It is found that turbine tower loads, in particular, are especially influenced by the earthquake excitation.

# Table of Contents

<b>Acknowledgments</b>	<b>v</b>
<b>Abstract</b>	<b>vi</b>
<b>List of Tables</b>	<b>xi</b>
<b>List of Figures</b>	<b>xiii</b>
<b>Chapter 1. Introduction</b>	<b>1</b>
1.1 Background . . . . .	1
1.2 Motivation . . . . .	2
1.3 Scope . . . . .	3
1.4 Thesis Organization . . . . .	4
<b>Chapter 2. Model Development for Turbine Response Simulation with Seismic Input</b>	<b>5</b>
2.1 Introduction . . . . .	5
2.2 Literature Review . . . . .	6
2.2.1 Models for Earthquake-Induced Loads . . . . .	6
2.2.2 Design Codes and Standards . . . . .	7
2.3 Simulation Model . . . . .	9
2.3.1 5-MW Baseline Wind Turbine Model . . . . .	10
2.3.2 Inflow Wind Velocity Fields . . . . .	13
2.3.3 Turbine Response Simulation . . . . .	13
2.3.4 Modeling Seismic Loads using FAST . . . . .	15
2.4 Earthquake Records used in the Current Study . . . . .	16
2.4.1 Binning of Ground Motion Records . . . . .	16
2.4.2 Normalization and Scaling of Earthquake Records . . . . .	19
2.4.3 Preparation of Earthquake Ground Motion Records . . . . .	20

2.4.4	Stochastic Response Simulations . . . . .	23
2.5	Summary . . . . .	25
<b>Chapter 3. Wind Turbine Response to Seismic Excitation</b>		<b>27</b>
3.1	Introduction . . . . .	27
3.2	Stochastic Response Simulations . . . . .	28
3.3	Statistical Analyses of Wind Turbine Loads . . . . .	28
3.3.1	Illustrative Time Series of Wind Input, Earthquake In- put, and Response Parameters . . . . .	28
3.3.2	Turbine Response Statistics . . . . .	33
3.3.2.1	Tower Base Fore-Aft Bending Moment . . . . .	34
3.3.2.2	Tower Base Side-to-Side Bending Moment . . . . .	45
3.3.2.3	Blade Root Out-of-Plane Moment . . . . .	46
3.3.3	Distribution of Response Extremes . . . . .	52
3.3.3.1	Tower Base Fore-Aft Bending Moment . . . . .	52
3.3.3.2	Tower Base Side-to-Side Bending Moment . . . . .	57
3.3.4	Power Spectral Density Functions . . . . .	62
3.3.5	Interpretation of Turbine Response Statistics . . . . .	70
3.3.6	Transients and Directionality . . . . .	73
3.3.6.1	Effects of Variation in Pre-earthquake Transient Period . . . . .	73
3.3.6.2	Effects of Orientation of Horizontal Ground Mo- tion Components . . . . .	75
3.4	Summary . . . . .	80
<b>Chapter 4. Conclusions</b>		<b>82</b>
4.1	Outline of Research Conducted . . . . .	82
4.2	Conclusions . . . . .	82
4.3	Future Research Prospects . . . . .	84
<b>Appendix</b>		<b>86</b>
<b>Appendix A. List of Ground Acceleration Records</b>		<b>87</b>
<b>Bibliography</b>		<b>93</b>



## List of Tables

2.1	Specifications related to the NREL 5-MW baseline wind turbine model. . . . .	11
2.2	Structural properties of the NREL 5-MW baseline wind turbine tower. [11] . . . . .	12
2.3	Natural frequencies of the turbine model with a fixed base and parked rotor. [18] . . . . .	16
2.4	Selected bins for the earthquake ground acceleration records. .	17
2.5	Western U.S. (California) earthquakes whose records were selected for this study. . . . .	19
2.6	Spectral acceleration normalisation levels for different earthquake bins used for the scaling of ground motion records. . . .	23
3.1	Summary statistics of the tower base fore-aft bending moment process from turbine response simulations with different scaling levels of the seismic input for a ground acceleration records from the ground motion bin with $M = 6.9$ and $R = 17.5$ km and for a hub-height mean wind speed, $V_w$ , equal to 10 m/s. . . . .	72
3.2	Extremes of the tower base fore-aft (TBsMyt) and side-to-side (TBsMxt) bending moments for varying transient periods for a ground acceleration record where $M = 6.9$ and $R = 13.0$ km and for a hub-height ten-minute mean wind speed, $V_w$ , equal to 10 m/s. . . . .	77
3.3	Extremes of the tower base fore-aft (TBsMyt) and side-to-side (TBsMxt) bending moments for varying orientations of the horizontal components of the input ground acceleration with respect to the wind turbine where the ground acceleration record is from a bin where $M = 6.9$ and $R = 13.0$ km and the hub-height ten-minute mean wind speed, $V_w$ , is equal to 10 m/s. . . . .	77
A.1	List of earthquake records used for ten-minute FAST simulations for the earthquake bin M1R1. . . . .	87
A.2	List of earthquake records used for ten-minute FAST simulations for the earthquake bin M1R2. . . . .	88

A.3	List of earthquake records used for ten-minute FAST simulations for the earthquake bin M1R3. . . . .	89
A.4	List of earthquake records used for ten-minute FAST simulations for the earthquake bin M2R1. . . . .	90
A.5	List of earthquake records used for ten-minute FAST simulations for the earthquake bin M2R2. . . . .	91
A.6	List of earthquake records used for ten-minute FAST simulations for the earthquake bin M2R3. . . . .	92

## List of Figures

2.1	Normalized response spectra of each of the 25 ground motion records of the earthquake bins – M1R1, M1R2, and M1R3 for two different normalizations. . . . .	21
2.2	Normalized response spectra of each of the 25 ground motion records of the earthquake bins – M2R1, M2R2, and M2R3 for two different normalizations. . . . .	22
2.3	Original and resampled time series of the three components of a ground acceleration record from the 1994 Northridge earthquake.	24
3.1	Time series of the hub-height longitudinal wind speed, the blade pitch angle, the ground accelerations in two horizontal orthogonal directions, the blade root in-plane and out-of-plane bending moments, and the tower base side-to-side and fore-aft bending moments. The time series are for a hub-height longitudinal mean wind speed, $V_w$ , equal to 10 m/s and for a ground acceleration record belonging to the M1R1 bin (Loma Prieta Earthquake: $M = 6.9$ , $R = 5.1$ km). . . . .	31
3.2	Time series (over the period from 290 to 400 seconds) of the hub-height longitudinal wind speed, the blade pitch angle, the ground accelerations in two horizontal orthogonal directions, the blade root in-plane and out-of-plane bending moments, and the tower base side-to-side and fore-aft bending moments. The time series are for a hub-height longitudinal mean wind speed, $V_w$ , equal to 10 m/s and for a ground acceleration record belonging to the M1R1 bin (Loma Prieta Earthquake: $M = 6.9$ , $R = 5.1$ km). . . . .	32
3.3	Ensemble statistics of tower base fore-aft bending moment extremes for ground motions belonging to different ground motion bins: (a) M1R1, (b) M1R2, and (c) M1R3, and for varying mean wind speeds at hub height. . . . .	36
3.4	Ensemble statistics of tower base fore-aft bending moment extremes for ground motions belonging to different ground motion bins: (a) M2R1, (b) M2R2, and (c) M2R3, and for varying mean wind speeds at hub height. . . . .	38

3.5	Ensemble statistics of tower base side-to-side bending moment extremes for ground motions belonging to different ground motion bins: (a) M1R1, (b) M1R2, and (c) M1R3, and for varying mean wind speeds at hub height. . . . .	42
3.6	Ensemble statistics of tower base side-to-side bending moment extremes for ground motions belonging to different ground motion bins: (a) M2R1, (b) M2R2, and (c) M2R3, and for varying mean wind speeds at hub height. . . . .	44
3.7	Ensemble statistics of blade root out-of-plane bending moment extremes for ground motions belonging to different ground motion bins: (a) M1R1, (b) M1R2, and (c) M1R3, and for varying mean wind speeds at hub height. . . . .	48
3.8	Ensemble statistics of blade root out-of-plane bending moment extremes for ground motions belonging to different ground motion bins: (a) M2R1, (b) M2R2, and (c) M2R3, and for varying mean wind speeds at hub height. . . . .	50
3.9	Distribution of extremes of the tower base fore-aft bending moment for the M1R1 ground motion bin for: (a) 1P frequency normalization; (b) tower fore-aft bending first-mode frequency normalization; and (c) cases with no earthquake input. . . . .	53
3.10	Distribution of extremes of the tower base fore-aft bending moment for the M1R2 ground motion bin for: (a) 1P frequency normalization; (b) tower fore-aft bending first-mode frequency normalization; and (c) cases with no earthquake input. . . . .	54
3.11	Distribution of extremes of the tower base fore-aft bending moment for the M2R1 ground motion bin for: (a) 1P frequency normalization; (b) tower fore-aft bending first-mode frequency normalization; and (c) cases with no earthquake input. . . . .	55
3.12	Distribution of extremes of the tower base fore-aft bending moment for the M2R2 ground motion bin for: (a) 1P frequency normalization; (b) tower fore-aft bending first-mode frequency normalization; and (c) cases with no earthquake input. . . . .	56
3.13	Distribution of extremes of the tower base side-to-side bending moment for the M1R1 ground motion bin for: (a) frequency normalization; (b) tower fore-aft bending first-mode frequency normalization; and (c) cases with no earthquake input. . . . .	58
3.14	Distribution of extremes of the tower base side-to-side bending moment for the M1R2 ground motion bin for: (a) frequency normalization; (b) tower fore-aft bending first-mode frequency normalization; and (c) cases with no earthquake input. . . . .	59

3.15	Distribution of extremes of the tower base side-to-side bending moment for the M2R1 ground motion bin for: (a) frequency normalization; (b) tower fore-aft bending first-mode frequency normalization; and (c) cases with no earthquake input. . . . .	60
3.16	Distribution of extremes of the tower base side-to-side bending moment for the M2R2 ground motion bin for: (a) frequency normalization; (b) tower fore-aft bending first-mode frequency normalization; and (c) cases with no earthquake input. . . . .	61
3.17	Power spectral density functions of the hub-height longitudinal wind speed, the ground acceleration in the longitudinal direction, the blade root out-of-plane moment, and the tower base fore-aft moment for a hub-height longitudinal mean wind speed, $V_w$ , equal to 10 m/s and ground motion input where $M = 6.9$ and $R = 13.0$ km. . . . .	64
3.18	Power spectral density functions of the hub-height longitudinal wind speed, the ground acceleration in the transverse direction, the blade root in-plane moment, and the tower base side-to-side moment for a hub-height longitudinal mean wind speed, $V_w$ , equal to 10 m/s and ground motion input where $M = 6.9$ and $R = 13.0$ km. . . . .	65
3.19	Power spectral density functions of the hub-height longitudinal wind speed, the ground acceleration in the longitudinal direction, the blade root out-of-plane moment, and the tower base fore-aft moment for four different ground motion records from the M1R1 bin and for a hub-height longitudinal mean wind speed, $V_w$ , equal to 10 m/s. . . . .	66
3.20	Power spectral density functions of the hub-height longitudinal wind speed, the ground acceleration in the longitudinal direction, the blade root out-of-plane moment, and the tower base fore-aft moment for four different ground motion records from the M1R1 bin and for a hub-height longitudinal mean wind speed, $V_w$ , equal to 12 m/s. . . . .	67
3.21	Power spectral density functions of the hub-height longitudinal wind speed, the platform acceleration in the transverse direction, the blade root in-plane moment, and the tower base side-to-side moment for four different ground motion records from the M1R1 bin and for a hub-height longitudinal mean wind speed, $V_w$ , equal to 10 m/s. . . . .	68
3.22	Power spectral density functions of the hub-height longitudinal wind speed, the platform acceleration in the transverse direction, the blade root in-plane moment, and the tower base side-to-side moment for four different ground motion records from the M1R1 bin and for a hub-height longitudinal mean wind speed, $V_w$ , equal to 12 m/s. . . . .	69

3.23	Time series (over the period from 290 to 340 seconds) of the tower base fore-aft moment for a hub-height longitudinal mean wind speed, $V_w$ , equal to 10 m/s, with no seismic input and with a fully 100% scaled seismic input motion for a ground motion bin with $M = 6.9$ and $R = 13.0$ km. . . . .	71
3.24	Power spectral density functions of the transverse and longitudinal ground acceleration components at different scaling levels [(a),(b)]; the longitudinal wind velocity at hub height [c]; the tower base fore-aft bending moment with no earthquake input [d]; and the tower-base fore-aft bending moment for 25%, 50%, 75%, and 100% scaling [(e), (f), (g), (h)] of a ground acceleration record from a bin with $M = 6.9$ and $R = 13$ km and for a hub-height mean ten-minute wind speed, $V_w$ , equal to 10 m/s. . . . .	74
3.25	Time series (over the period from zero to 200 seconds) of the tower base fore-aft and side-to-side bending moments for a hub-height longitudinal wind speed, $V_w$ , equal to 10 m/s and for a ground motion record where $M = 6.9$ and $R = 13.0$ km with different transient periods prior to ground shaking that vary from 20 to 100 seconds. . . . .	76
3.26	Time series (over the period from 290 to 450 seconds) of the tower base fore-aft and side-to-side bending moment for a hub-height longitudinal wind speed, $V_w$ , equal to 10 m/s, and for a ground motion record where $M = 6.9$ and $R = 13.0$ km for alternate orientations of the horizontal components of the input ground acceleration with respect to the wind turbine. . . . .	78

# Chapter 1

## Introduction

### 1.1 Background

In order to diversify the global energy portfolio and meet increasing energy demands, a significant development of renewable sources of energy especially wind energy has been witnessed in recent decades. Wind turbine technology has developed tremendously over the past years. Within the United States of America, at the end of 2010, the installed capacity of wind power was over 40,000 MW. Wind power accounts for about 3% of the electricity generated within the United States. Wind energy plays a pivotal role in satisfying the increasing energy demands of various states in the country. In California, where earthquakes often occur, wind power plays a vital role in the state's electricity portfolio. In 2007, turbines installed in that state generated 6,802 gigawatt-hours of electric energy, approximately 2.3% of the state's gross system energy.

In considering structural loads on a wind turbine, even in seismically active regions such as California, seismic loads are regarded as less important compared to wind-induced aerodynamic loads. Seismic loads, however, should assume greater importance for wind turbines installed in regions where earthquakes occur. Within the U.S., the United States Geological Survey (USGS) provides seismic hazard maps for use in the design of civil infrastructure. A systematic loads analysis of turbines based on seismic hazard deaggregation

for specific turbine sites should be an integral part of the site assessment and structural integrity analysis of a turbine. In order to execute such seismic analyses, various simplified approaches have been employed in the past. However, in recent years, the focus has shifted from superposition of separate seismic and aerodynamic loads analyses to wind turbine numerical simulation studies that take into account seismic and aerodynamic loads together. Such simulation approaches can provide insight into the coupled dynamics of a turbine and account, for example, for the effects of aerodynamic and structural damping on turbine loads. Various simplified as well as complex simulation models have been used in the seismic analyses of turbine loads in recent studies. The present study involves an exhaustive and comprehensive seismic analysis of the “National Renewable Energy (NREL) 5-MW Baseline Wind Turbine” model based on stochastic simulation for a suite of potential controlling earthquake events representative of sites in the Western U.S. The ground motion records chosen (that represent specified event magnitude and distance from rupture) are used to characterize and study the dynamic response of the turbine and the resulting extreme loads.

## 1.2 Motivation

The IEC 61400-1 Ed.3: Wind turbines design - Part 1: Design requirements [10]; the Risø-Det Norske Veritas (Risø-DNV) Guidelines for Design of Wind Turbines [22]; and the Germanischer Lloyd (GL) Guidelines for the certification of wind turbines [7] provide recommendations for the seismic design of wind turbines. In regions of high seismic activity, it is necessary to perform a thorough seismic analysis. Available standards provide simplified

frequency-domain and time-domain analysis procedures to assess turbine tower loads for two cases—normal operation and emergency shutdown. The available standards present only a very generalized approach to the required seismic analyses.

Several different models for describing seismic loads on wind turbines have been published in recent years. Prowell et al. [19] present a comprehensive review of the literature regarding various simplified and full-system wind turbine models used for seismic analysis of turbine loads. Among these models, one that uses the open-source software, FAST, and its seismic modeling capability allows time-domain simulation of the turbine response including earthquake ground motion input along with aerodynamic force computation. The use of such time-marching simulation procedures, that employ as input available ground motion records (i.e., ground acceleration time series) for a specific site, allows a designer to develop site-specific turbine loads.

### 1.3 Scope

This study focuses on developing a thorough understanding of the dynamic characteristics and extreme loads on a wind turbine during a seismic event. Extreme loads that result from three orthogonal components of ground acceleration input excitation during normal operation of the NREL 5-MW baseline wind turbine are addressed here; aerodynamic loads are inherently coupled with the seismic input and are included in the analyses. To gain an understanding of turbine response/load extremes for different geographical regions, ground acceleration records associated with different event magnitudes and distances from fault rupture (and, hence, of different peak ground acceler-

ation levels and different spectral acceleration demand levels) are considered. A statistical study of the extreme turbine response is presented in this study.

## 1.4 Thesis Organization

This thesis comprises four chapters. Chapter 2 provides a literature review of published seismic models used in wind turbine loads studies; it also provides a brief description of the wind turbine model, the computational procedure and the open-source software, and the reference sites selected that are defined by seismic event characteristics such as magnitude and distance to rupture. The filtering, resampling, normalization, and scaling processes used for preparation of the earthquake ground acceleration data for subsequent computational studies are also described. Chapter 3 discusses turbine response statistics based on time-domain simulations for a range of different wind field inputs and ground acceleration records. Turbine response time series, power spectra, and statistics are discussed in detail. Chapter 4 summarizes the study objectives and highlights the key results and conclusions of this study.

## Chapter 2

# Model Development for Turbine Response Simulation with Seismic Input

### 2.1 Introduction

The design of wind turbines at locations of high seismic activity needs to take into consideration site-specific characteristics of ground motions that can occur there. In loads analyses, it is important that simulations of turbine response be carried out for all operating states of the turbine and with simultaneous consideration of seismic input as well as aerodynamic loading. Design standards and industry guidelines—such as IEC 61400-1 Ed.3: Wind turbines design - Part 1: Design requirements [10]; Guidelines for Design of Wind Turbines [22]; and Guidelines for the certification of wind turbines [7]—discuss how such loads analyses may be performed. They, however, provide only a very generalized approach to analysis of wind turbines for seismic input; this is because earthquakes are of concern only in some regions and because it is generally felt that aerodynamic loads dominate the overall turbine response. A number of simplified and full-system wind turbine models that incorporate seismic loading have been developed in recent years. Many of these models allow for time-domain simulation of a full-system turbine subject to seismic input excitation. A comprehensive simulation study using earthquake ground acceleration records with varying magnitude, distance to fault rupture, peak Ground Acceleration (PGA) levels, etc. can be utilized to gain insight into

the turbine dynamics.

In Chapter 1, a description of the motivating factors and scope of the current research work was provided. The present chapter provides a review of prior studies related to the modeling of seismic excitation on wind turbines. Current design code provisions for seismic analysis of wind turbines are also discussed. Furthermore, the turbine response simulation model, a stochastic 3-D turbulent wind field, and the procedure for selection and processing of ground motion records from the Western United States—all of which are needed for the loads analyses including seismic inputs that are part of the present study—are discussed in this chapter.

## **2.2 Literature Review**

A number of models for wind turbine loads analysis that incorporate seismic inputs have been developed in recent years. Results from these studies and current code provisions for the seismic design of wind turbines are discussed in this section.

### **2.2.1 Models for Earthquake-Induced Loads**

Prowell and Veers [19] presented an insightful analysis of the literature describing various simplified and full-system wind turbine models that have been published and used for the seismic analysis of turbines. Bazeos et al. [4] and Lavassas et al. [15] presented extensive finite element models for prototype turbines with power ratings of 450 kW and 1 MW, respectively. Both these studies employed simple single-degree-of-freedom models with the rotor

and nacelle mass lumped at the top of the tower. In order to assess the influence of seismic loads on wind turbine components other than the tower, Ritschel et al. [20] proposed the use of a simplified distributed mass cantilever beam model for a 2.5 MW turbine. Witcher [23] discussed the importance of time-domain simulations while accounting for aeroelastic interactions by using Garrad Hassan's program, Bladed. A hybrid rigid-flexible multibody system (MBS) model [25], [26] (though not explicitly developed for earthquake inputs); the software, Simulation of Wind Energy Converters (SIWEC), developed by Windrad Engineering [8]; and the open-source software, FAST, with capabilities introduced for modeling seismic loads on wind turbines [18] are examples of computational frameworks developed for turbine loads analyses. Studies by Riziotis et al. [21], Hansen et al. [9], and Prowell et al. [17] discuss results from numerical and experimental investigations that deal with the effects of aerodynamic damping on turbine loads and response. Results from these studies suggest a dependence of the amount of aerodynamic damping on the mean wind speed; as well, the directionality of strongest seismic input will be influenced by the presence and amount of this aerodynamic and turbine loads resulting from differently aligned wind and dominant seismic signals will be affected by this damping.

### **2.2.2 Design Codes and Standards**

Design standards and industry guidelines such as IEC 61400-1 Ed.3: Wind turbines design - Part 1: Design requirements [10]; Guidelines for Design of Wind Turbines [22]; and Guidelines for the Certification of Wind Turbines [7] address seismic design. In regions of high seismic hazard, it is essential

to perform a thorough seismic analysis for turbine loads. The standards provide only a generalized view on the methodologies to be employed for such seismic analysis.

The Risø guidelines [22] propose the use of a lumped-mass model for seismic analysis; the nacelle mass, the rotor mass, and a quarter of the tower mass are lumped at the top of the tower. The resulting natural period of this lumped-mass system is the basis to select the spectral acceleration from the site-specific design response spectrum to establish the seismic loads acting on the turbine tower. The standard provides no guidelines, however, for the appropriate levels of damping to be used for the frequency-domain seismic analysis of the proposed single-degree-of-freedom system. Also, it is assumed that appropriate building code provisions will be employed for deriving design loads using the calculated spectral acceleration, as no procedure is provided for such calculations.

The Germanischer Lloyd (GL) guidelines [7] propose either the application of local building codes or the American Petroleum Institute [3] recommendation. Earthquakes with a return period of 475 years are prescribed to be used as the design level earthquake. It is suggested that at least the first three modes of vibration must be considered for both time-domain and frequency-domain analyses and that a minimum of six simulations must be performed for each load case for the time-domain analysis. The seismic loads resulting from the frequency-domain or the time-domain analyses are prescribed to be combined with the loads due to other environmental conditions and that a factor of 1.0 be applied to the seismic loads. As with the Risø guidelines [22], the GL guidelines provide no specifications regarding the levels of structural or aerodynamic damping to be assumed.

The IEC design standard [10] also prescribe requirements for seismic

analysis of wind turbines. In accordance with the GL guidelines [7], the IEC standard also prescribes the use of an earthquake event with a return period of 475 years for the seismic analysis of the turbine. It allows both frequency-domain and time-domain analyses that account for consecutive modes that make up a modal mass that is 85% of the total mass. Elastic response of the turbine is assumed although energy dissipation in ductile deformation may be assumed for specific structural systems such as lattice structures as well as in bolted joints. The resulting loads from the seismic analysis are superimposed with the greater of (i) the lifetime-averaged operating loads; or (ii) the emergency shutdown loads. Annex C in the IEC standard provides a simplified procedure to compute a conservative estimate of the tower seismic loads. According to the procedure, a design response spectrum from site-specific building codes adjusted for a damping ratio of 1% may be used to establish the design response acceleration based on the first tower mode period. Tower base shear and moments are then computed by applying, at the top of the tower, a force equal to the total mass of the rotor, the nacelle, and half of the tower mass times the design response acceleration. The guidelines prohibit superposition of seismic loads with the larger of lifetime-averaged operating loads and emergency shutdown loads if seismic excitation causes significant loading in structural elements of the turbine other than the tower.

### **2.3 Simulation Model**

In the present study, we employ the open-source software, FAST (Fatigue, Aerodynamics, Structures, and Turbulence) [14], developed at the National Renewable Energy Laboratory, for the wind turbine response simula-

tions. The FAST code is a software tool that can be used to model two-bladed and three-bladed horizontal-axis wind turbines (HAWTs) under various environmental conditions; it can thus be used to estimate extreme and fatigue loads. The 3-dimensional inflow turbulent wind field is simulated using TurbSim [12], which is used in conjunction with FAST. We describe details regarding the 5-MW NREL baseline wind turbine model, the inflow turbulence simulation, structural modeling in FAST, and the ground motion modeling using FAST.

### **2.3.1 5-MW Baseline Wind Turbine Model**

The NREL 5-MW baseline wind turbine model was developed at the National Wind Technology Center (NWTC) based on the specifications of a representative utility-scale multi-megawatt wind turbine [11]. The wind turbine model is a conventional three-bladed, variable-speed, collective pitch-controlled upwind turbine developed to support conceptual studies. The structural and mechanical properties of the turbine are based on various documents published by turbine manufacturers with a special emphasis on the REpower 5M turbine. The turbine model consists of a cantilevered 87.6 m high tower; the hub is 90 m above the ground. The tower's base diameter is 6 m and its thickness at the base is 0.027 m. It tapers linearly towards the top, where the diameter and the thickness reduce to 3.87 m and 0.019 m, respectively. Mechanical properties of the tower are based on effective steel properties with a Young's modulus of 210 GPa, a shear modulus of 80.8 GPa, and an effective density of 8,500 kg/m<sup>3</sup>. The rotor diameter is 126 m. The turbine has a rated rotor rotation rate of 12.1 rpm and the rated wind speed is 11.4 m/s.

Table 2.1: Specifications related to the NREL 5-MW baseline wind turbine model.

Turbine Type	Horizontal Upwind Wind Turbine
Power Rating	5 MW
Control Type	Variable-Speed, Collective-Pitch Control
Hub Height	90 m
Tower Height	87.6 m
Rotor Diameter	126 m
Blade Length Along Pre-coned Axis	61.5m
Tower Mass	347,460 kg
Nacelle Mass	240,000 kg
Rotor Mass	111,000 kg
Rated Rotor Speed	12.1 RPM
Rotor Speed Range	6.9 RPM to 12.1 RPM
Cut-in Wind Speed	3 m/s
Cut-out Wind Speed	25 m/s
Rated Wind Speed	11.4 m/s

The integrated tower mass is 347,460 kg; its center of mass (C.M.) is located 38.234 m above the ground along its centerline. The damping ratio for all the vibrational modes of the tower is specified at 1% of the critical damping ratio. Table 2.1 presents a summary of various specifications related to the NREL 5-MW baseline wind turbine model. Table 2.2 presents a summary of the structural properties of the NREL 5-MW baseline wind turbine tower. This NREL 5-MW baseline wind turbine model is the subject of the present study.

Table 2.2: Structural properties of the NREL 5-MW baseline wind turbine tower. [11]

Elevation above ground (m)	Mass Distribution (kg/m)	Flexural Rigidity $EI$ (N-m <sup>2</sup> )	Torsional Rigidity $GJ$ (N-m <sup>2</sup> )	Axial Rigidity $EA$ (N)	Moment of Inertia (kg-m <sup>2</sup> )
0	5590.87	614.34E+9	472.75E+9	138.13E+9	24866.3
8.76	5232.43	534.82E+9	411.56E+9	129.27E+9	21647.5
17.52	4885.76	463.27E+9	356.5E+9	120.71E+9	18751.3
26.28	4550.87	399.13E+9	307.14E+9	112.34E+9	16155.3
35.04	4227.75	341.88E+9	263.09E+9	104.45E+9	13838.1
43.80	3916.41	291.01E+9	223.94E+9	96.76E+9	11779.0
52.56	3616.83	246.03E+9	189.32E+9	89.36E+9	9958.2
61.32	3329.03	206.46E+9	158.87E+9	82.25E+9	8356.6
70.08	3053.01	171.85E+9	132.24E+9	75.43E+9	6955.9
78.84	2788.75	141.78E+9	109.10E+9	68.90E+9	5738.6
87.60	2536.27	115.82E+9	89.13E+9	62.66E+9	4688.0

### 2.3.2 Inflow Wind Velocity Fields

The software, TurbSim [12], is used to simulate the 3-dimensional inflow wind velocity field for the turbine response simulations. TurbSim generates zero-mean longitudinal ( $u$ ), lateral ( $v$ ), and vertical ( $w$ ) components of the turbulent wind field over a 2-dimensional grid spanning the rotor plane. In each simulation, TurbSim adds a non-zero mean wind velocity component to the longitudinal component of the turbulent wind field. Kaimal power spectral density functions are used to simulate time series for the three components of the turbulent wind field. An exponential coherence function is employed to describe the coherence of the longitudinal wind velocity component at different frequencies and for different spatial separations. The expected value of the turbulence intensity at the turbine site is assumed to be 0.14 for a 15 m/s mean wind speed at hub height. This expected value of turbulence intensity is consistent with medium turbulence category B; the actual turbulence intensity varies with the mean wind speed at hub height in accordance with IEC 61400-1 [10]. The simulated 3-dimensional stochastic turbulent wind velocity field as described is used to compute aerodynamic forces on the blades using routine, AeroDyn, which is incorporated in the open-source software, FAST.

### 2.3.3 Turbine Response Simulation

The program, FAST, models two-bladed and three-bladed horizontal-axis wind turbines as multi-degree-of-freedom systems in the time domain. The turbine is modeled as a combination of rigid and flexible bodies. Five flexible bodies are used to describe the tower, the three blades, and the drive shaft; there are additionally nine rigid bodies. A total of 24 degrees of free-

dom (DOFs) can be used to describe the turbine model. These include three translational and three rotational DOFs of the platform in three orthogonal directions; the first two fore-aft and first two side-to-side bending modes of the flexible tower; the yawing motion of the nacelle, the azimuth angle of the generator, the drivetrain compliance, the first two in-plane and out-of-plane bending modes of each of the three blades, the rotor furl, and the tail furl modes. Only 19 of the possible 24 degrees of freedom are used in the present study. We do not employ the three rotational degrees of freedom of the platform, the rotor furl, and the tail furl modes; these are kept inactive during the FAST time-marching simulations. Both the tower and the three blades that are modeled as flexible bodies are assumed to deform as a combination of their respective modes. We employ an active blade pitch controller during the FAST simulations of the 5MW wind turbine model. This active blade pitch control causes turbine loads to vary as a function of the mean wind speed at hub height by limiting the aerodynamic loads on the turbine while maintaining constant power output at mean wind speeds greater than the rated wind speed [1], [2]. Hence, this active blade pitch control plays an important role in influencing turbine load distributions relative to the hub-height mean wind speed.

As stated, the FAST software employs a combined multi-body and modal dynamics formulation with five flexible bodies. The nacelle, being considerably stiffer than the other turbine components, is modeled as a rigid body. The tower and blade mode shapes are externally calculated and described by five-coefficient sixth-order polynomials of the form:

$$\Phi(x) = a_1x^2 + a_2x^3 + a_3x^4 + a_4x^5 + a_5x^6 \quad (2.1)$$

where  $x$  refers to the spatial coordinate, from the fixed end describing the cantilevered tower or blade, normalized with respect to its length; the coefficients,  $a_i$ , in Equation 2.1 sum to unity. Note that no constant and linear coefficients appear in the mode shape expressions as they are equal to zero under the cantilever assumption. The overall stiffness of the turbine system is derived using the mode shapes and the distributed stiffness matrices.

### 2.3.4 Modeling Seismic Loads using FAST

Recent updates to the FAST open-source software [13] allow for the modeling of an offshore wind turbine placed on a dynamic platform. This feature has been employed to input ground accelerations caused by an earthquake to the tower base platform at each time step of a time-marching simulation [18]. It is thus possible to simulate seismic ground motion in conjunction with a 3-dimensional turbulent wind field instead of having to superimpose environmental and earthquake loads as has been the situation in many earlier studies.

The earthquake excitation is generally described by means of time histories for the ground acceleration, velocity, or displacement. In the FAST simulations for seismic loads, the ground acceleration time histories along three orthogonal axes during the earthquake need to be provided. At each integration step of the time-marching procedure, a damped oscillator attached to the base of the turbine platform is simulated to calculate the force required to achieve the desired ground acceleration time history. Prowell et al. [18] recommend setting the natural frequency of the damped oscillator to twice the highest frequency found in the ground acceleration time histories along

Table 2.3: Natural frequencies of the turbine model with a fixed base and parked rotor. [18]

Mode	Frequency Hz
1 <sup>st</sup> Tower Fore-Aft	0.32
1 <sup>st</sup> Tower Side-to Side	0.31
1 <sup>st</sup> Blade Asymmetric Flapwise Yaw	0.67
1 <sup>st</sup> Blade Asymmetric Flapwise Pitch	0.67
1 <sup>st</sup> Blade Collective Flap	0.70
1 <sup>st</sup> Blade Asymmetric Edgewise Pitch	1.08
1 <sup>st</sup> Blade Asymmetric Edgewise Yaw	1.09
2 <sup>nd</sup> Tower Fore-Aft	2.90
2 <sup>nd</sup> Tower Side-to-Side	2.93
2 <sup>nd</sup> Blade Asymmetric Flapwise Yaw	1.93
2 <sup>nd</sup> Blade Asymmetric Flapwise Pitch	1.92

the three orthogonal axes. For accurate reproduction of these ground motion time histories, it is also recommended to use a damping ratio that is 65% of critical for the damped oscillator. This model is employed in the present study for the simulation of seismic loads on the NREL 5-MW baseline wind turbine model using FAST. Table 2.3 presents various natural frequencies of the turbine model.

## 2.4 Earthquake Records used in the Current Study

### 2.4.1 Binning of Ground Motion Records

We have discussed details regarding the modeling of seismic loads on the NREL 5-MW baseline wind turbine using FAST time-marching analysis. In

Table 2.4: Selected bins for the earthquake ground acceleration records.

Bin	Magnitude, $M$	Distance from Fault Rupture, $R$ (km)
M1R1	$M > 6.5$	$0 < R \leq 20$
M1R2	$M > 6.5$	$20 < R \leq 40$
M1R3	$M > 6.5$	$R > 40$
M2R1	$5.0 < M \leq 6.5$	$0 < R \leq 20$
M2R2	$5.0 < M \leq 6.5$	$20 < R \leq 40$
M3R3	$5.0 < M \leq 6.5$	$R > 40$

this work, both near-field and far-field strong motion records from the Western United States are used to simulate and analyze the influence of earthquake ground motions on a wind turbine. For the purposes of a comparative study, the selected earthquake records were classified into six different bins on the basis of the moment magnitude of the earthquake, and the distance to the fault rupture. The ground acceleration records were first divided into two sets—one, where the moment magnitudes,  $M$ , is greater than 6.5 and another where  $M$  lies between 5.0 and 6.5. These sets were further divided on the basis of the shortest distance of the recording station from the fault rupture,  $R$ . The two magnitude-based record sets were divided into three bins each, based on the shortest distance,  $R$ , of the recording station from the fault rupture as follows:  $R \leq 20$  km;  $20 < R \leq 40$  km; and  $R > 40$  km, respectively. In summary, the ground acceleration records were divided into six different bins based on  $M$  and  $R$ . Table 2.4 provides a summary of the selected bins for the earthquake records.

A total of twenty-five different earthquake records were selected for each of the six bins. For this purpose, the Pacific Earthquake Engineering Research Center (PEER) strong motion database was used to identify suitable

ground acceleration records from various Western U.S. earthquakes. Table 2.5 provides a list of the Western U.S. earthquakes (all from California) that were considered for this study. These include the 1994 Northridge Earthquake ( $M$  6.7), the 1989 Loma Prieta Earthquake ( $M$  7.1), the 1979 Imperial Valley Earthquake ( $M$  6.5), and the 1992 Landers Earthquake ( $M$  7.3) among others.

The selection of ground motion records from among those available was greatly influenced by the spectral acceleration of the records at important frequencies related to the turbine dynamics. As described in Table 2.3, the natural frequencies of vibration of wind turbine structural components are significantly smaller than those of typical civil engineering structures. While screening records for each bin, a requirement was placed that the larger of the two horizontal components' peak ground acceleration (PGA) had to be at least 0.1g (this larger component was applied in the longitudinal direction of the wind turbine). However, the PGA requirements were relaxed to 0.07g for the far field earthquake bins—i.e., M1R3 and M2R3. As stated, the natural frequencies for different modes of vibration of the wind turbine are quite low; they generally lie in the constant-velocity region of a seismic response spectrum and correspond to relatively lower spectral acceleration levels than at higher frequencies. Ground acceleration records were selected as long as they showed sufficient spectral acceleration levels at important low frequencies for the wind turbine. In particular, all the ground acceleration records were screened such that they had sufficiently high spectral acceleration values at the 1P frequency of the turbine rotor (i.e., at the rotor rotation rate of 0.2 Hz or 12.1 rpm) and at the tower fore-aft first mode frequency. Appendix A provides a bin-wise list of all the records that were used in this study.

Table 2.5: Western U.S. (California) earthquakes whose records were selected for this study.

ID	Magnitude	Year	Name
1	7.1	1992	Cape Mendocino
2	7.3	1992	Landers
3	7.1	1989	Loma Prieta
4	6.7	1994	Northridge
5	6.6	1971	San Fernando
6	5.9	1986	Chalfant Valley
7	5.7	1979	Coyote Lake
8	6.5	1979	Imperial Valley
9	6.2	1984	Morgan Hill
10	6.1	1966	Parkfield
11	6.0	1987	Whittier Narrows
12	6.3	1987	Superstition Hills
13	6.3	1967	Northern California

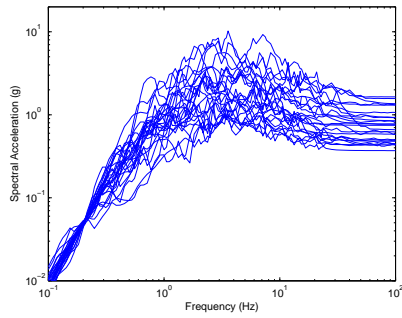
#### 2.4.2 Normalization and Scaling of Earthquake Records

The selected ground acceleration records in each bin were normalized or scaled to have consistent spectral acceleration values at specified frequencies. The first normalizing basis was taken as the mean of the spectral acceleration (of the larger horizontal components of the selected ground motions in a bin) at the turbine’s 1P frequency (1P Normalization (1PN)). This 1P frequency refers to the frequency at which the rotor makes one complete revolution. This frequency at which the rotor rotates is governed by the control system of the turbine. At rated power, the turbine rotates at the rated rotor speed—i.e., at 12.1 rpm or approximately 0.2 Hz—when hub-height wind speeds are at or above the rated wind speed. For wind speeds below the rated wind speed, the rotor rotates at a frequency below the rated speed—i.e., at lower than 0.2

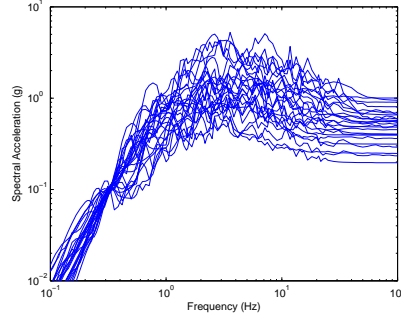
Hz. To account for this variation of the rotor speed with wind speed (various wind speeds were considered in simulations that included seismic input motions), the earthquake ground acceleration records were normalized to the spectral acceleration level corresponding to an average of the spectral acceleration at a group of frequencies about 0.2 Hz. A second normalizing basis for the ground motion records was taken as the mean of the spectral acceleration (of the larger horizontal components of the selected ground motions in a bin) at the tower first fore-aft modal frequency—i.e., at 0.32 Hz (tower base normalization(TBN)). Scaling of the ground motion records in each bin to the basis (mean 1P or mean first tower fore-aft mode frequency) was necessary; only those ground acceleration records were selected where the scale factor to normalize the records was between 0.2 and 5 so as to avoid artificially altering the original recorded motion excessively. Table 2.6 provides the scaling levels of the spectral acceleration at both the normalization frequencies for different earthquake bins. Figures 2.1 and 2.2 present the scaled response spectra for each of the twenty-five records of all the earthquake bins at the two different normalizations.

### 2.4.3 Preparation of Earthquake Ground Motion Records

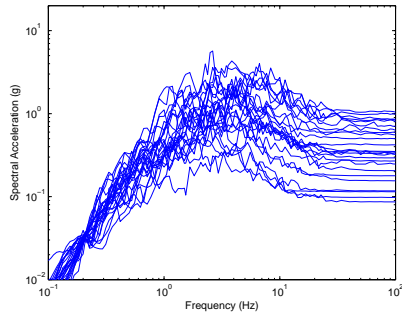
In a previous study [18], it was established that turbine response simulations of earthquake ground acceleration records with FAST produced stable results for integration time steps equal to 0.002 seconds. In the present study, FAST simulations were executed with integration time steps varying between 0.001 and 0.005 seconds. The simulations executed with time steps up to 0.003 seconds produced stable results for different earthquake ground motion records; for integration time steps greater than 0.003 seconds, non-convergent



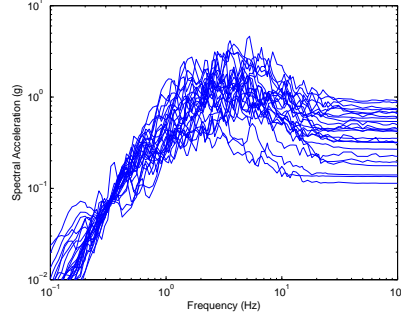
(a) M1R1 - 1P Normalization



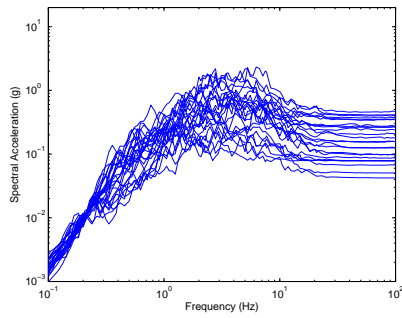
(b) M1R1 - Tower Base Normalization



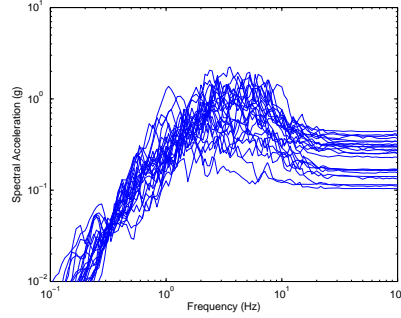
(c) M1R2 - 1P Normalization



(d) M1R2 - Tower Base Normalization

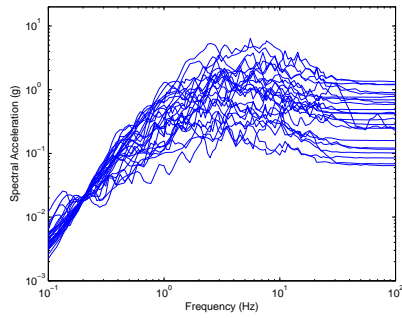


(e) M1R3 - 1P Normalization

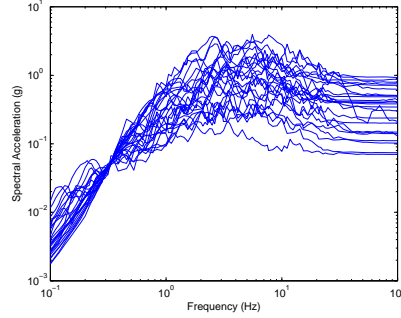


(f) M1R3 - Tower Base Normalization

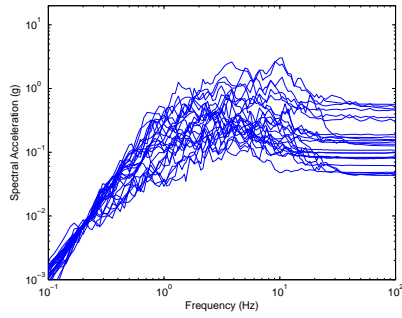
Figure 2.1: Normalized response spectra of each of the 25 ground motion records of the earthquake bins – M1R1, M1R2, and M1R3 for two different normalizations.



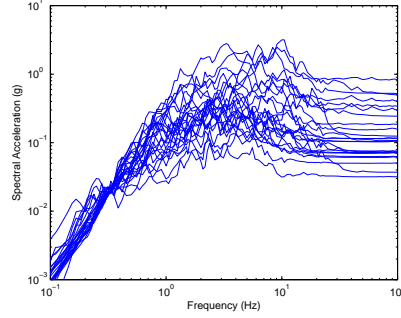
(a) M2R1 - 1P Normalization



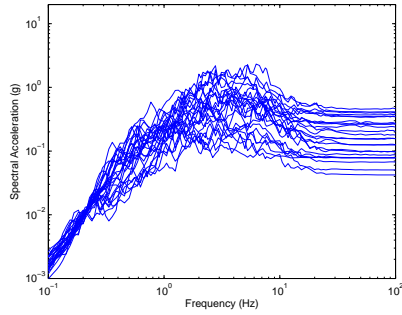
(b) M2R1 - Tower Base Normalization



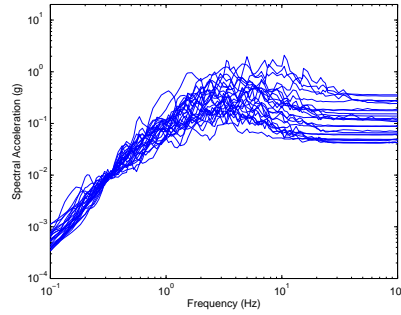
(c) M2R2 - 1P Normalization



(d) M2R2 - Tower Base Normalization



(e) M2R3 - 1P Normalization



(f) M2R3 - Tower Base Normalization

Figure 2.2: Normalized response spectra of each of the 25 ground motion records of the earthquake bins – M2R1, M2R2, and M2R3 for two different normalizations.

Table 2.6: Spectral acceleration normalisation levels for different earthquake bins used for the scaling of ground motion records.

EQ Bin	Normalization Levels	
	1P Normalization (1PN)	Tower Base Fore-Aft Frequency Normalization (TBN)
M1R1	0.05g	0.1g
M1R2	0.03g	0.07g
M1R3	0.01g	0.04g
M2R1	0.02g	0.05g
M2R2	0.007g	0.02g
M2R3	0.004g	0.01g

numerical integration resulted. Hence, an integration time step of 0.002 seconds was chosen for the time-marching FAST turbine response simulations. A polyphase filter was used to resample the normalized earthquake ground acceleration records. During the resampling process, an anti-aliasing (low-pass) Finite Impulse Response (FIR) filter was applied to each time series. Each of the records was thus upsampled to a sampling rate of 500Hz. Figure 2.3 shows the original and resampled time series for the three components of a ground acceleration record from the 1994 Northridge earthquake. The time series for the original and the resampled ground acceleration motion show very slight differences.

#### 2.4.4 Stochastic Response Simulations

Following the processing of the ground acceleration records, fifteen ten-minute turbine response simulations were conducted for each normalized

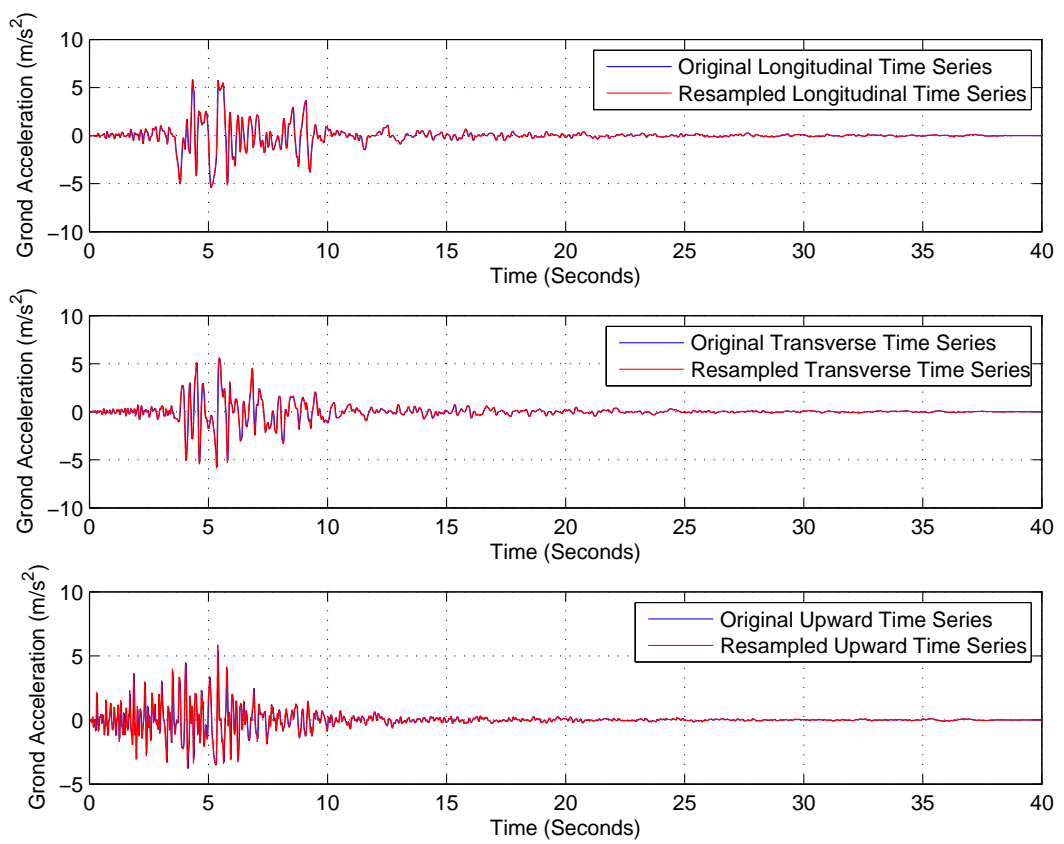


Figure 2.3: Original and resampled time series of the three components of a ground acceleration record from the 1994 Northridge earthquake.

ground motion record for all the six bins listed in Appendix A while varying the 3-D turbulent wind field by considering different mean wind speeds at hub height, ranging from cut-in to cut-out wind speeds. Thus, a total of 54,000 simulations were run for all the normalized ground motion records. Note that the fifteen ten-minute simulations for the two different normalized ground motion records at a given wind speed employed the same fifteen 3-D turbulent wind fields as the seeds for the TurbSim input were conserved so as to facilitate comparison studies. For the same fifteen ten-minute 3-D turbulent wind field inputs at each of the different mean wind speeds, the turbine response was also simulated without any earthquake input. This was done so as to facilitate comprehensive quantification of the influence of the seismic loading contribution to various turbine response parameters.

## 2.5 Summary

In this chapter, we presented a brief literature review of wind turbine models used for seismic load analysis. Today's standards and guidelines that address seismic design for wind turbines (such as in IEC 61400-1 Ed.3: Wind turbines design - Part 1: Design requirements [10]; Guidelines for Design of Wind Turbines [22]; and Guidelines for the certification of wind turbines [7]) were also discussed. The NREL 5-MW baseline wind turbine model was presented in detail along with information on the structural and mechanical properties of the turbine. Recent developments in the open-source software, FAST, that allow modeling of seismic loads in conjunction with aerodynamic loads were described along with the simulation models employed in the current study. Finally, the ground motion records selection process, their

binning, their normalization and scaling, and record resampling techniques were described. Statistical analysis of the results of the time-marching turbine response simulations executed using FAST for different earthquake records are discussed next.

## Chapter 3

# Wind Turbine Response to Seismic Excitation

### 3.1 Introduction

In Chapter 2, a survey of the literature concerning models for wind turbine loads analysis for seismic input was presented and current design code provisions were discussed. The NREL 5-MW baseline wind turbine model was presented along with details related to the structural and mechanical properties of the turbine. Refinements made to the open-source software, FAST, that allow modeling of seismic loads in conjunction with aerodynamic loads were described as were details related to selected ground motion records considered in this study. In this chapter, we present a statistical study of the dynamically coupled seismic-aerodynamic response of the selected wind turbine in the time domain for various ground motion records and various inflow wind fields. The procedure for selection of ground motion records of different event magnitude and distance to rupture, their binning, and the processing of these records before their use in the response computations were discussed earlier. Results from the turbine response simulations are presented in the form of statistical summaries of the extremes of tower and blade loads. Time series and power spectra are also analyzed. Finally, the issues of wind versus earthquake directionality and transients in the response computation are discussed by studying results from FAST turbine response simulations.

## 3.2 Stochastic Response Simulations

Fifteen ten-minute simulations of the turbine response were carried out for each of the selected ground acceleration records listed in Appendix A, for the two normalization procedures discussed in Chapter 2, and for mean wind speeds at hub height varying from cut-in to cut-out. In each ten-minute simulation, the 3-D turbulent wind field generated using TurbSim was input to FAST along with three components of ground acceleration starting at 300 seconds and continuing for the duration of the ground acceleration record, which varied from one record to another. During the latter portion of the simulation (i.e., following the ground shaking), the turbine response simulation was continued with wind input only and the effects of the seismic input were allowed to gradually damp out. The turbine response time series data were employed in statistical analyses of various load parameters. Details and results of the statistical analysis are discussed in the following sections.

## 3.3 Statistical Analyses of Wind Turbine Loads

### 3.3.1 Illustrative Time Series of Wind Input, Earthquake Input, and Response Parameters

To illustrate various features of the simulation studies carried out, for a single magnitude-distance bin (M1R1), a scaled record from the Loma Prieta earthquake ( $M = 6.9$ ,  $R = 5.1$  km) is discussed where a turbulent wind field with a hub-height ten-minute mean wind speed of 10 m/s is also simulated. Time series for various turbine loads are presented in Figure 3.1 along with the simulated hub-height longitudinal wind speed and the two horizontal components of the ground acceleration. The figure shows normalized time

series data such that for each process,  $y(t)$ , what is shown is the variation of  $y_{norm}(t) = (y(t) - E[y(t)]) / \max[\text{abs}(y(t))]$  with time,  $t$ , over the ten minutes of the FAST response simulation. The various time series presented include the longitudinal wind speed at hub height (WindVxi), the blade pitch angle (Bld-Pitch), the platform acceleration in the longitudinal direction (PtfmTAxt), the platform acceleration in the transverse direction (PtfmTAyt) (these platform accelerations effectively describe the ground accelerations in the longitudinal and transverse directions), the blade root in-plane bending moment (RootMxc1), the blade root out-of-plane bending moment (RootMyc1), the tower base side-to-side bending moment (TBsMxt), and the tower base fore-aft bending moment (TBsMyt). As can be seen in the time series, during this ten-minute simulation, the wind turbine is operating at a longitudinal mean wind speed of 10 m/s for the first 300 seconds so as to remove any transient effects of start-up. The earthquake ground accelerations are then input and they continue for a duration of approximately 40 seconds. Over the remaining 260 seconds, the turbine continues to operate at the same mean wind speed at hub height; the turbine response due to the earthquake input is allowed to damp out and decay with time. A similar procedure is used for all the turbine response simulations where the duration of the ground acceleration inputs vary from one record to another. Note that the input ground motions have been scaled based on the normalization and scaling procedure described in Chapter 2 (either the 1P rotor rotation rate or the tower first mode fore-aft natural frequency is the basis for the scaling of the ground motions in each bin).

A closer observation of the time series presented in Figure 3.1 suggests that there is significant high-frequency energy evident in the tower base fore-aft and side-to-side bending moments. Figure 3.2 presents the same time series as in Figure 3.1 but focused on a 110-second portion of the record that contains

the entire duration of ground shaking together with portions before and after the shaking. The tower base moment time series show that extremes of these tower loads are clearly driven by the seismic input and that the fore-aft and side-to-side moments are driven predominantly by the longitudinal and transverse components of ground acceleration, respectively. Thus, there is a clear dynamic interaction between the ground accelerations and the turbine loads. Note too that the fore-aft tower base moment decays much faster than the side-to-side tower base moment; this is because of the additional aerodynamic damping in the longitudinal direction which is aligned with the horizontal (longitudinal) component of the earthquake that drives the fore-aft tower moments. In the transverse direction of earthquake motion which affects the side-to-side tower base bending moment, the response is seen to decay more slowly; this is because the structural damping ratio assumed for the tower is only 1%, as was discussed in Chapter 2.

Unlike the tower loads, the blade root in-plane and out-of-plane bending moments show more complex dynamic characteristics, around the period of intense ground shaking, that reflect contributions from both the wind and the ground motion. The time series for these two blade moments suggest a dominant influence of the turbulent wind and a relatively smaller influence of the ground motion; this is likely because only a limited portion of the ground shaking effect is carried to the blade root via motion of the tower. The maximum tower base fore-aft and side-to-side bending moments are found to be 156.7 MN-m and 88.2 MN-m, respectively; similarly, the maximum blade root in-plane and out-of-plane bending moments are found to be 5.9 MN-m and 13.5 MN-m, respectively.

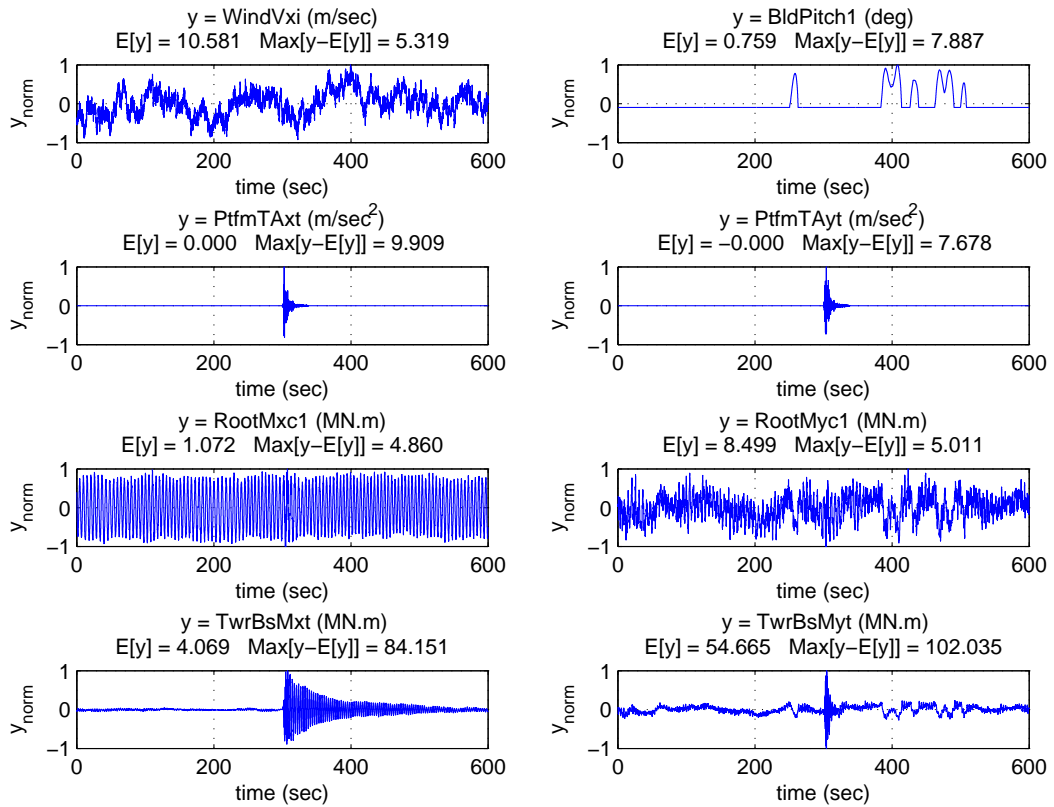


Figure 3.1: Time series of the hub-height longitudinal wind speed, the blade pitch angle, the ground accelerations in two horizontal orthogonal directions, the blade root in-plane and out-of-plane bending moments, and the tower base side-to-side and fore-aft bending moments. The time series are for a hub-height longitudinal mean wind speed,  $V_w$ , equal to 10 m/s and for a ground acceleration record belonging to the M1R1 bin (Loma Prieta Earthquake:  $M = 6.9$ ,  $R = 5.1$  km).

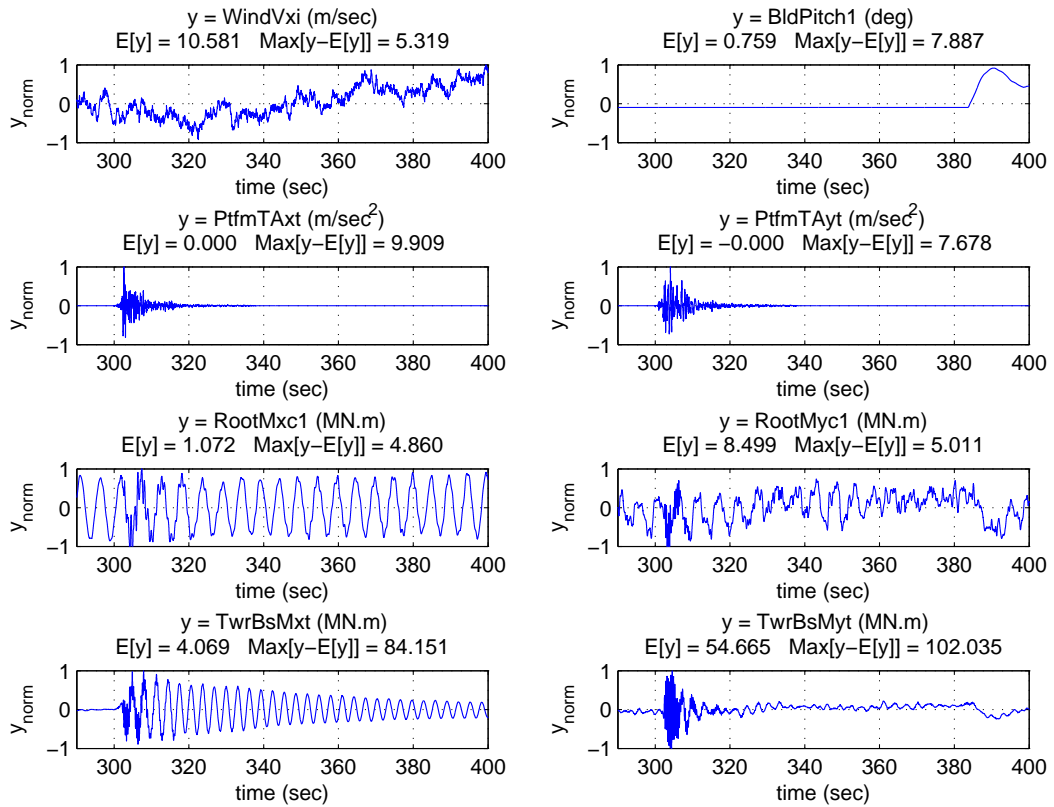


Figure 3.2: Time series (over the period from 290 to 400 seconds) of the hub-height longitudinal wind speed, the blade pitch angle, the ground accelerations in two horizontal orthogonal directions, the blade root in-plane and out-of-plane bending moments, and the tower base side-to-side and fore-aft bending moments. The time series are for a hub-height longitudinal mean wind speed,  $V_w$ , equal to 10 m/s and for a ground acceleration record belonging to the M1R1 bin (Loma Prieta Earthquake:  $M = 6.9$ ,  $R = 5.1$  km).

### 3.3.2 Turbine Response Statistics

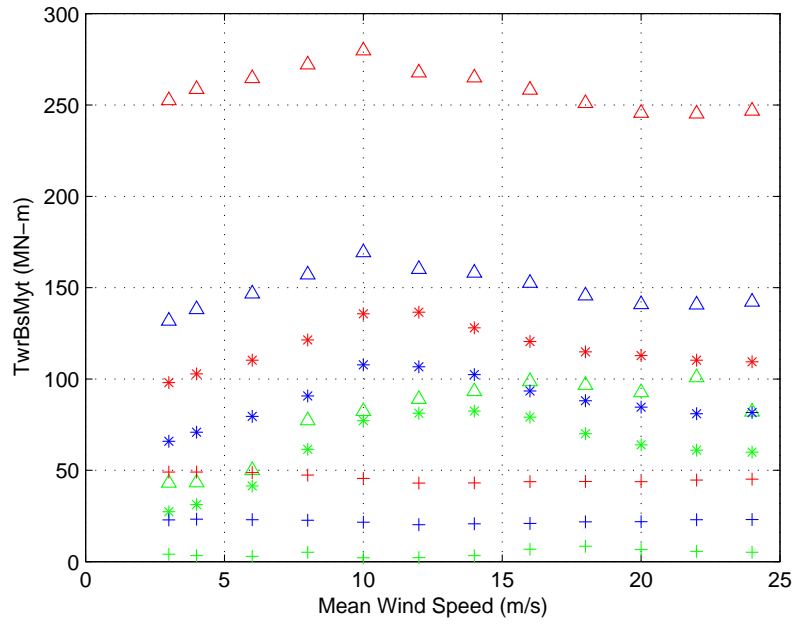
In order to study the effects of seismic events on the structural loads of a wind turbine, the present study characterizes the earthquake ground motions on the basis of the moment magnitude of the earthquake and the distance to the fault rupture by dividing these motions into six different bins. To compare the effects of different ground acceleration records on the loading parameters, a limited number of simulations have been conducted with the records of each bin normalized to spectral accelerations at one of two different frequencies—the rotor 1P frequency (1P Normalization (1PN)) or the tower fore-aft first mode frequency (tower base normalization (TBN)). To quantify the relative contribution of the various seismic motions from different  $M$ - $R$  bins versus the wind input (with different mean values at hub height) on loads, it is of interest to study load extremes as a function of the different earthquake  $M$ - $R$  bins and the different hub-height mean wind speeds. The rationale for studying scaled ground motions where the scaling was tied to important frequencies (such as the rotor 1P frequency or the tower fore-aft first mode frequency) is that since these frequencies are likely to be dominant in energy in the turbine response, scaling the motions to the same level there would enable us to study if earthquake loads with similar levels of input at these frequencies would lead to less variability in load extremes or not. Note that the simulations performed may be used to identify those earthquake  $M$ - $R$  bins and wind speed combinations that cause the greatest turbine loads on average. The simulations may also be used to evaluate wind-earthquake combinations that lead to greater load variability. Variability in load extremes directly affects the tails of the distribution of the turbine load parameters; combinations of specific earthquake ground motion types and specific wind speeds even with comparatively lower

extremes on average can control extreme loads distributions if variability in loads is high for those wind-earthquake combinations.

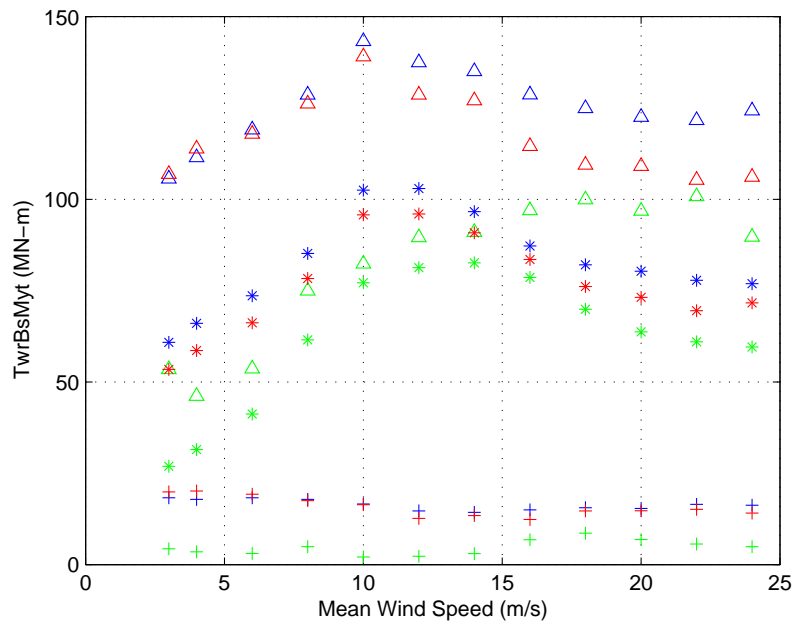
In order to study extreme response/load values during a ten-minute simulation, it is important to evaluate the occurrence of maxima of the turbine load parameter,  $X$ , in question—for example,  $X$  can represent the tower base fore-aft bending moment (TBsMyt), the tower base side-to-side bending moment (TBsMxt), a blade root out-of-plane bending moment (RootMyc), or a blade root in-plane bending moment (RootMxc), during the simulation. Thus, for each bin, it is useful to examine the distribution of ensemble maxima of load parameters based on the records in that bin. At each mean wind speeds between cut-in and cut-out, fifteen turbulent wind fields were simulated and each set of these fifteen were combined with twenty-five ground motion records for each bin (with two different ground motion normalizations—1PN and TBN). A single ensemble maximum (largest of the  $25 \times 15$  simulations at each wind speed for each normalization) and the mean and standard deviation of the ten-minute maxima were studied for different load parameters,  $X$ .

### 3.3.2.1 Tower Base Fore-Aft Bending Moment

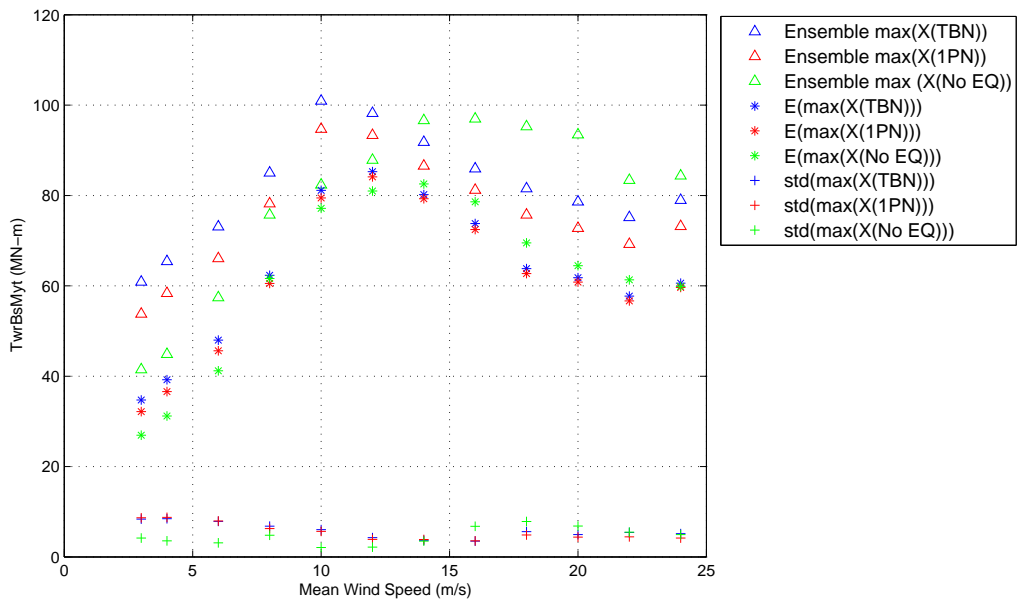
Figures 3.3 and 3.4 summarize ensemble statistics of extreme values of the tower base fore-aft bending moment for ground motions belonging to the six different  $M$ - $R$  bins for different mean wind speeds at hub height. The ensemble overall maxima (i.e., the largest extreme from  $25 \times 15$  or 375 simulations at each wind speed), as well as the mean (expected) extremes of the fore-aft moment, increase with wind speed starting from the cut-in wind speed—i.e., 3 m/s. The largest bending moment values occur at a hub-height



(a) Earthquake Bin: M1R1

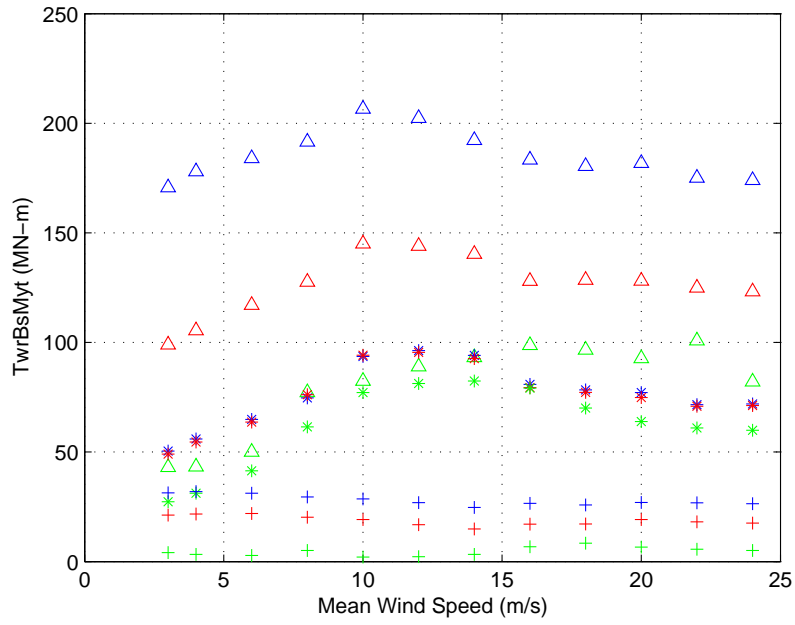


(b) Earthquake Bin: M1R2

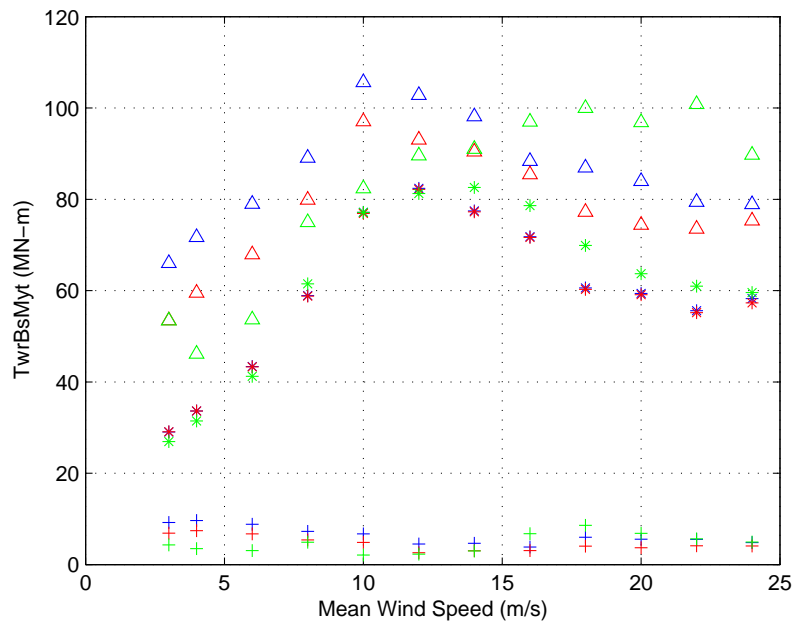


(a) Earthquake Bin: M1R3

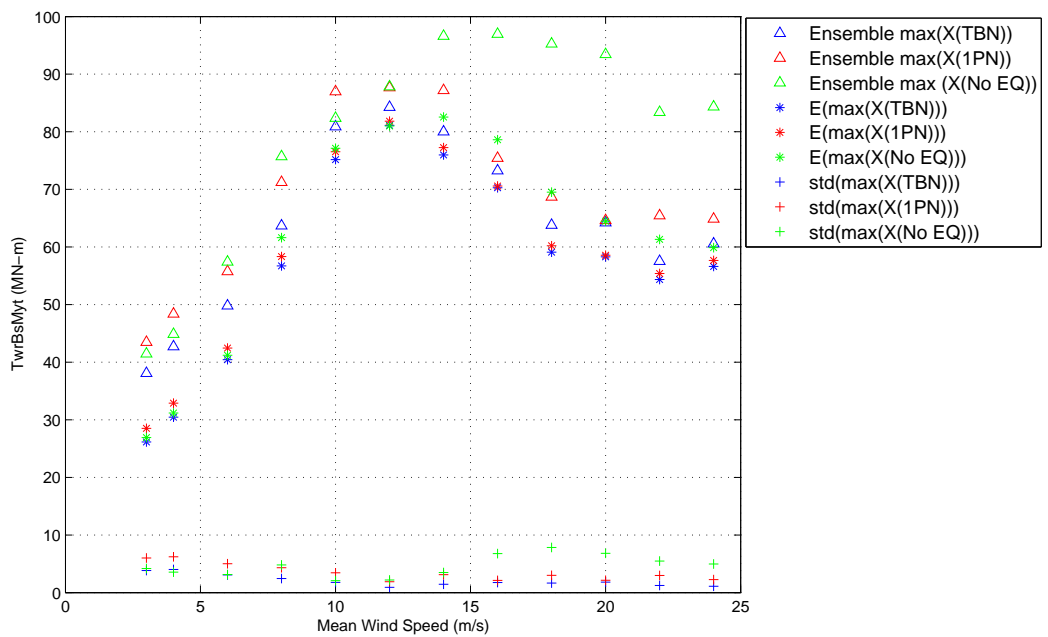
Figure 3.3: Ensemble statistics of tower base fore-aft bending moment extremes for ground motions belonging to different ground motion bins: (a) M1R1, (b) M1R2, and (c) M1R3, and for varying mean wind speeds at hub height.



(a) Earthquake Bin: M2R1



(b) Earthquake Bin: M2R2



(a) Earthquake Bin: M2R3

Figure 3.4: Ensemble statistics of tower base fore-aft bending moment extremes for ground motions belonging to different ground motion bins: (a) M2R1, (b) M2R2, and (c) M2R3, and for varying mean wind speeds at hub height.

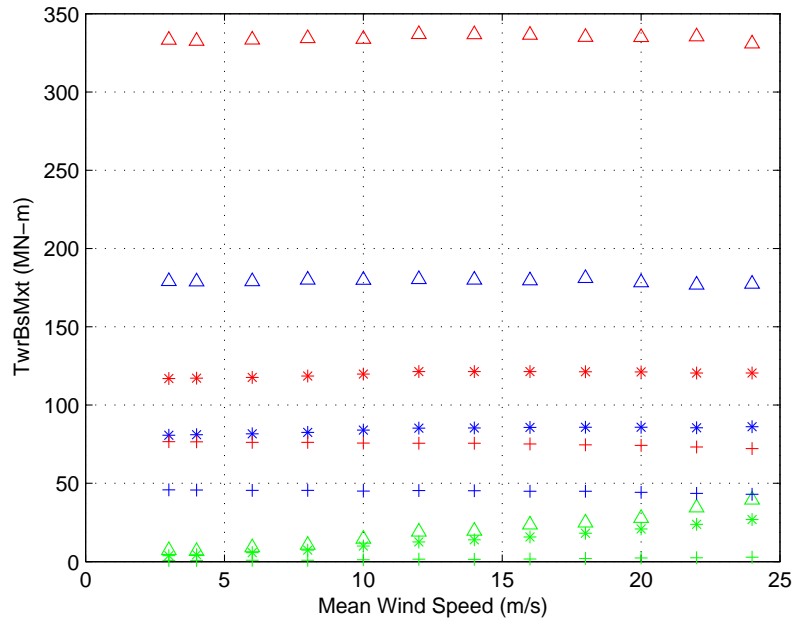
ten-minute mean wind speed of 10 m/s. For mean wind speeds greater than 11.4 m/s (the rated wind speed), ensemble maxima as well as expected values of the extremes of the fore-aft moment decrease. This is attributed to the pitch control characteristics of the wind turbine. The ten-minute load extremes vary significantly with magnitude and distance of the ground motions considered. The largest ensemble maxima as well as the largest mean extremes are associated with larger magnitude earthquakes. Load maxima at a given mean wind speed also show significant variation with changes in the distance,  $R$ , of the recording station from the fault rupture. Bins with ground motions recorded closer to the fault rupture yielded higher load maxima on average. Variability in tower load extremes appeared to be smaller at larger distances.

For the M1R1 bin, the 25-sample ensemble maximum of the tower base fore-aft moment is observed to be 185.3 MN-m and 279.8 MN-m, respectively, for normalizations based on the tower fore-aft first mode frequency (TBN) of 0.32 Hz (scaled to 0.1g) and on the 1P frequency (1PN) of 0.2 Hz (scaled to 0.05g). Despite the common earthquake records in these two cases and the same 3-dimensional turbulent wind field, the ensemble maxima of the tower base fore-aft bending moment for these two different normalizations differ by 94.5 MN-m. As described earlier, the ground acceleration records were chosen so as to limit the scale factors for all the records to lie between 0.2 and 5.0, so as to maintain the realistic nature of the motions as recorded. The variation in the ensemble maxima occurs due to the differences in the normalization procedures and the scale factors applied to the individual records in each bin; this emphasizes the point that the normalization of ground acceleration records based on spectral acceleration at a specified frequency (to have similar demand/input levels at that important frequency) for the purpose of a comparative study plays an important role in the estimation of extreme loads.

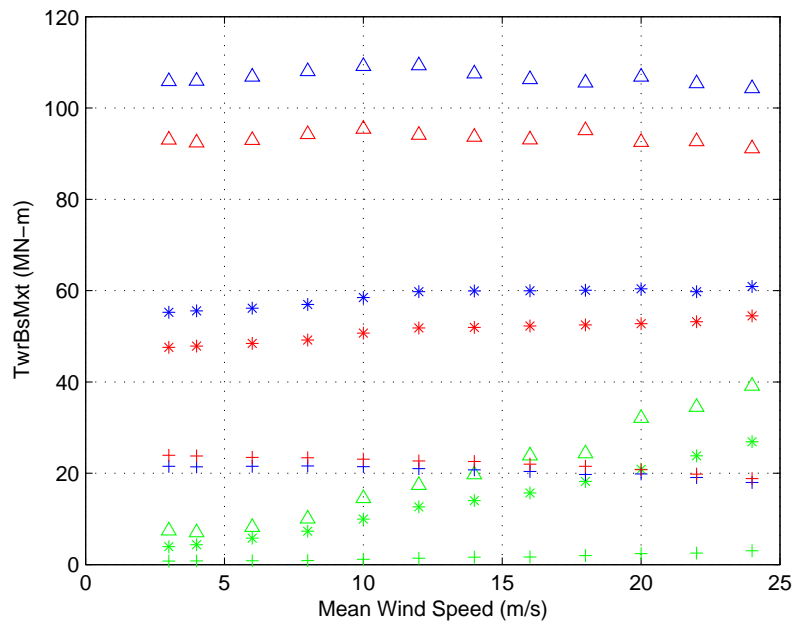
Similar results and trends as for the M1R1 bin are observed for other earthquake ground acceleration bins when studying ensemble maximum as well as expected extremes of the tower base fore-aft moment; these extremes decrease with a reduction in  $M$  and an increase in  $R$ .

For a given mean wind speed, an increase in standard deviation estimates of the extreme tower base fore-aft moment is observed as  $M$  increases and  $R$  decreases—in these cases, a higher input energy from the ground motion record causes an increase in the variability of the load extremes. For example, the standard deviation of the extreme tower base fore-aft bending moment at a mean wind speed of 10 m/s increases from 16.6 to 21.5 MN-m when going from M1R2 to M1R1 (i.e., with decreasing distance) for the TBN case. It is partly because of these differences in standard deviation and variability in load extremes that the ensemble and expected extremes are more widely separated for ground motions with higher  $M$  and lower  $R$  values. For the tower base fore-aft extremes, standard deviation estimates show relatively low sensitivity to the mean wind speed; these standard deviation estimates remain relatively constant for mean wind speeds up to the rated wind speed. For wind speeds above the rated wind speed, a slight reduction in the standard deviation estimates is observed up to a mean wind speed of 16 m/s; further increase in the mean wind speed at hub height causes a slight increase in these estimates.

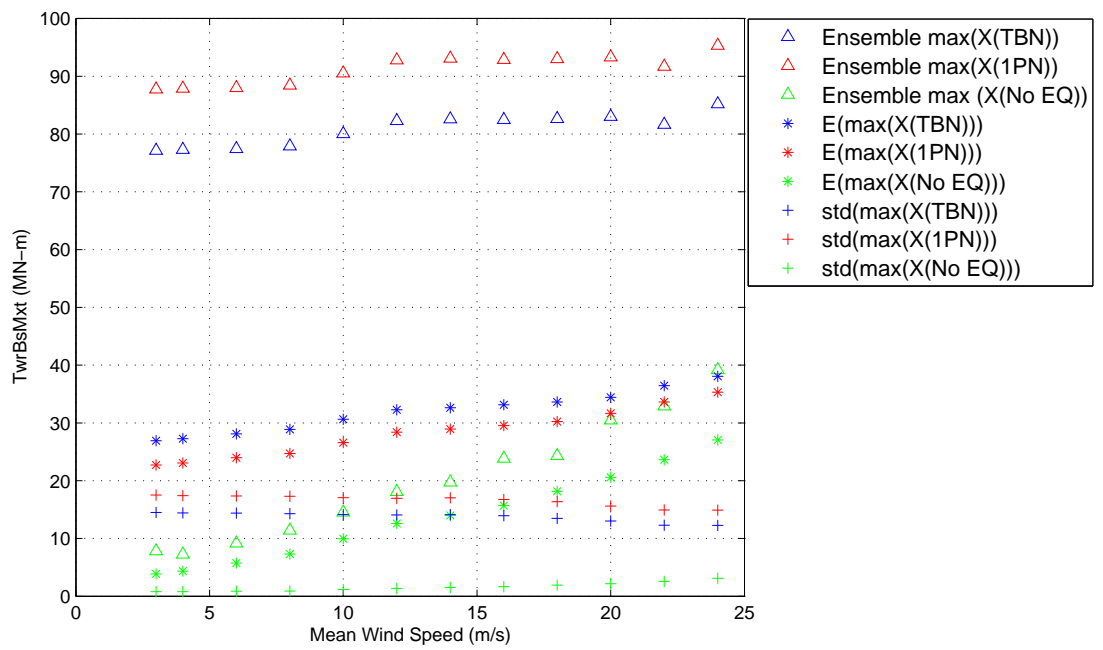
Figures 3.3 and 3.4 suggest that in the absence of the earthquake input, the tower base fore-aft extreme bending moment is considerably smaller than when seismic input excitation is included. This is true for all the  $M$ - $R$  ground motion bins.



(a) Earthquake Bin: M1R1

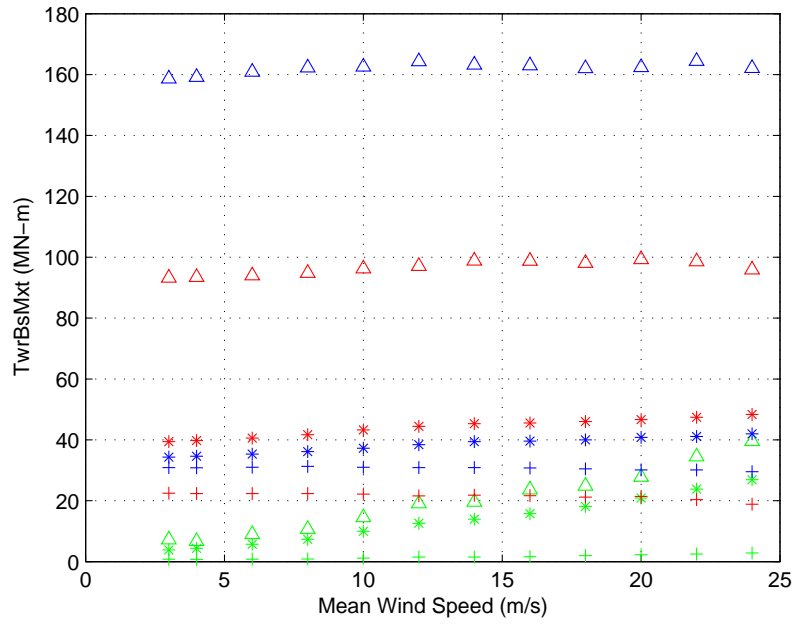


(b) Earthquake Bin: M1R2

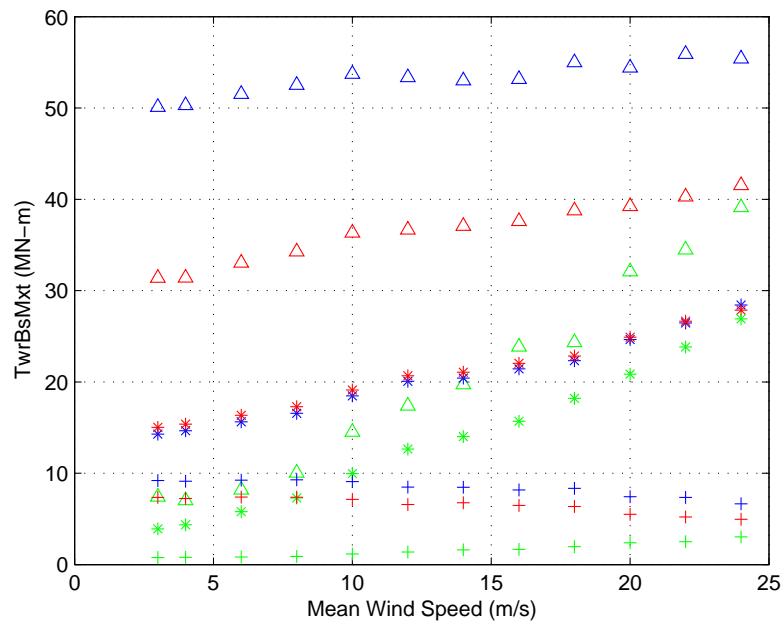


(a) Earthquake Bin: M1R3

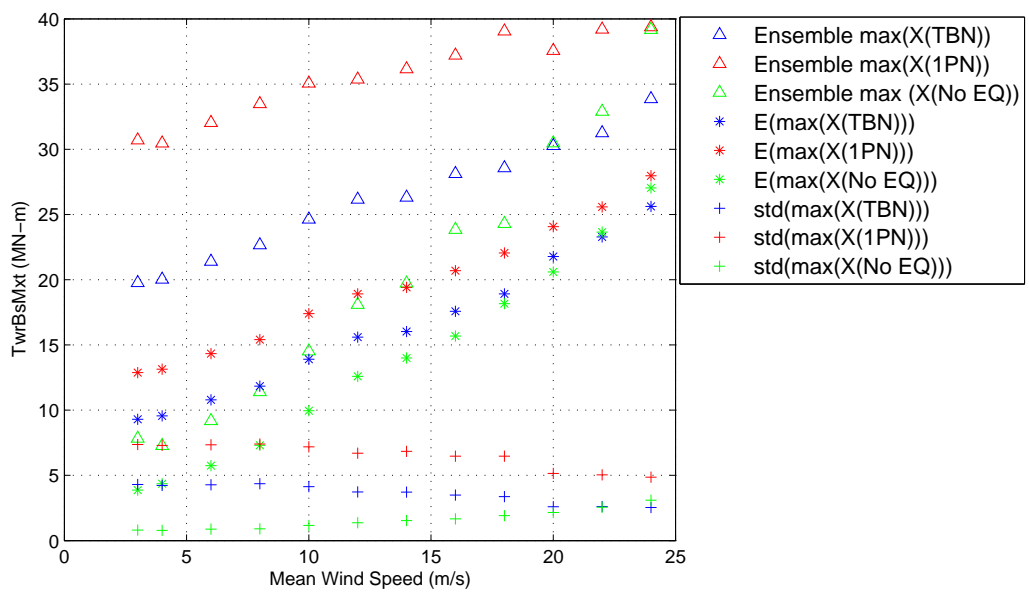
Figure 3.5: Ensemble statistics of tower base side-to-side bending moment extremes for ground motions belonging to different ground motion bins: (a) M1R1, (b) M1R2, and (c) M1R3, and for varying mean wind speeds at hub height.



(a) Earthquake Bin: M2R1



(b) Earthquake Bin: M2R2



(a) Earthquake Bin: M2R3

Figure 3.6: Ensemble statistics of tower base side-to-side bending moment extremes for ground motions belonging to different ground motion bins: (a) M2R1, (b) M2R2, and (c) M2R3, and for varying mean wind speeds at hub height.

### 3.3.2.2 Tower Base Side-to-Side Bending Moment

Figures 3.5 and 3.6 summarize statistics of the extreme tower base side-to-side bending moment for ground motions belonging to the six different bins and for different mean wind speeds at hub height. The ensemble overall maxima as well as the mean extremes of the tower base side-to-side moment do not show significant variation with the mean wind speed at hub height. Similar to the tower base fore-aft moment, the ensemble maxima as well as the expected maxima vary considerably with variation in  $M$  and  $R$ . The largest ensemble maxima (overall) and the largest expected maxima are associated with higher  $M$  and lower  $R$  values.

The lack of variation in the tower base side-to-side bending moment extremes with mean wind speed is because this load is not driven by the mean wind field in the longitudinal direction. The load extremes show significant variation from one ground motion bin to another; this suggests that the ground acceleration input greatly influences the tower base side-to-side moment. For the M1R1 bin, the ensemble maximum overall is estimated to be 180.4 MN-m and 333.9 MN-m for the TBN and 1PN cases, respectively. Similar to the tower base fore-aft moment, some variation in the load maxima results with the two alternative normalization procedures because of the different scale factors used for the individual records in each ground motion bin. Similar results (to those for the M1R1 bin) are obtained for the other earthquake ground acceleration bins when studying tower side-to-side extreme bending moments; in general, these extremes decrease with a reduction in  $M$  and an increase in  $R$ .

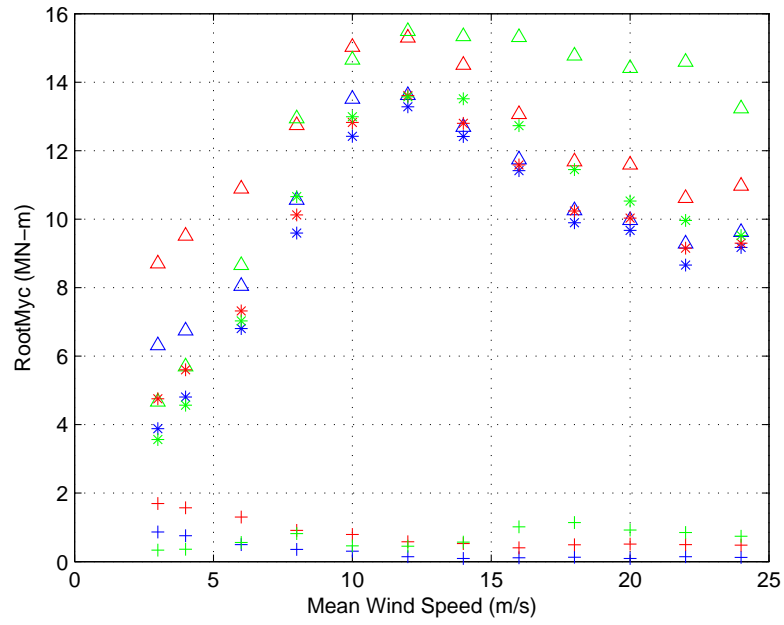
An increase in standard deviation estimates of the load extremes are observed as  $M$  increases and  $R$  decreases. Again, this increase occurs due to the relative increase in input energy from near-field high-magnitude ground

motion recordings. These standard deviation estimates at a mean wind speed of 10 m/s increase from 21.4 MN-m to 45.1 MN-m when going from the M1R2 to M1R1 for the TBN case. Extremes of the tower base side-to-side moment exhibit greater variability for ground accelerations with a higher  $M$  and a lower  $R$ . These standard deviation estimates show relatively low sensitivity to the mean wind speed at hub height. Also these standard deviation estimates remain relatively constant for mean wind speeds up to the rated wind speed; beyond the rated wind speed, a slight reduction is observed up to a mean wind speed of 16 m/s.

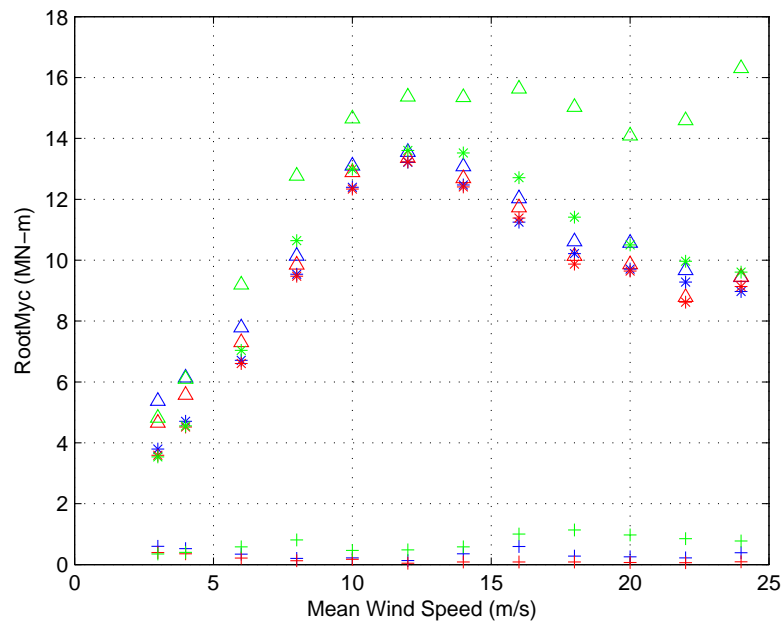
Figures 3.5 and 3.6 suggest that in the absence of the earthquake input, the tower base side-to-side extreme bending moment is considerably smaller than when seismic input excitation is included. This is true for all the  $M$ - $R$  ground motion bins.

### 3.3.2.3 Blade Root Out-of-Plane Moment

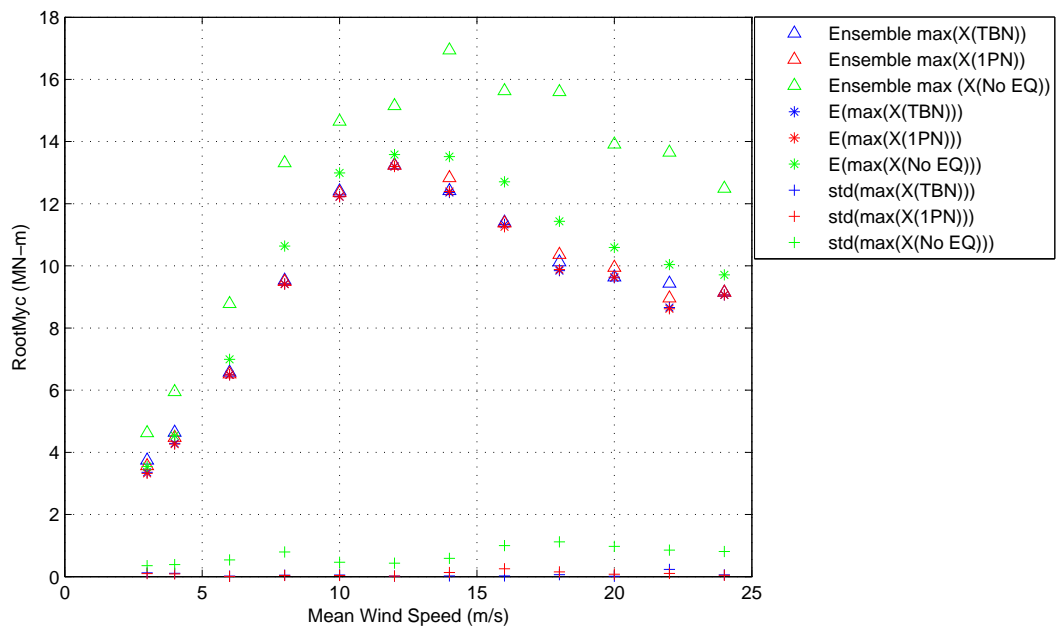
Figures 3.7 and 3.8 summarize statistics of the extreme blade root out-of-plane bending moment for ground motions belonging to the six different bins and for different mean wind speeds. The ensemble overall maxima as well as the mean extremes of the blade root out-of-plane moment increase with increase in wind speed above the cut-in wind speed. The largest extremes occur at a mean wind speed of 10 m/s. For mean wind speeds above the rated wind speed, the ensemble maxima as well as expected values of the blade moment extremes decrease with increase in mean wind speed. Again, this is a result of the pitch-control characteristics of the turbine. In a few situations, large load extremes are observed for mean wind speeds close to the cut-out wind speed. Interestingly, out-of-plane blade root bending moment extremes do not vary



(a) Earthquake Bin: M1R1

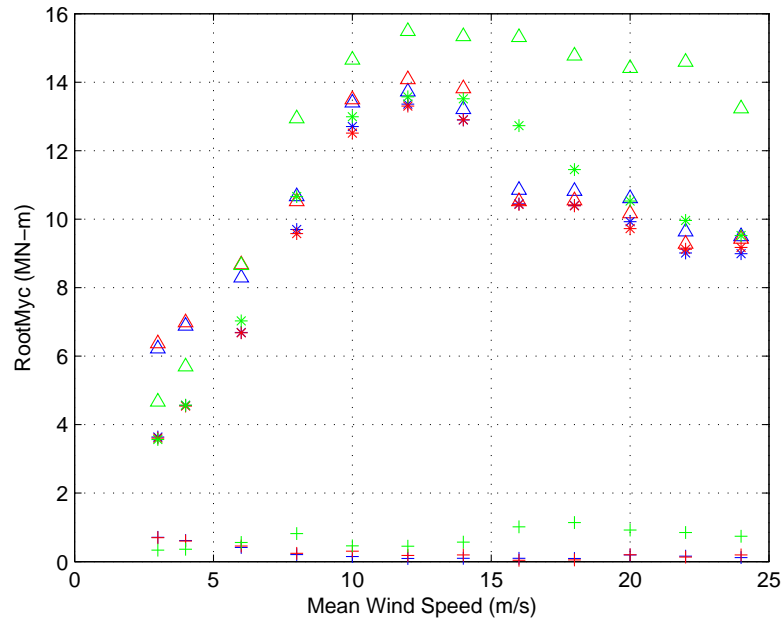


(b) Earthquake Bin: M1R2

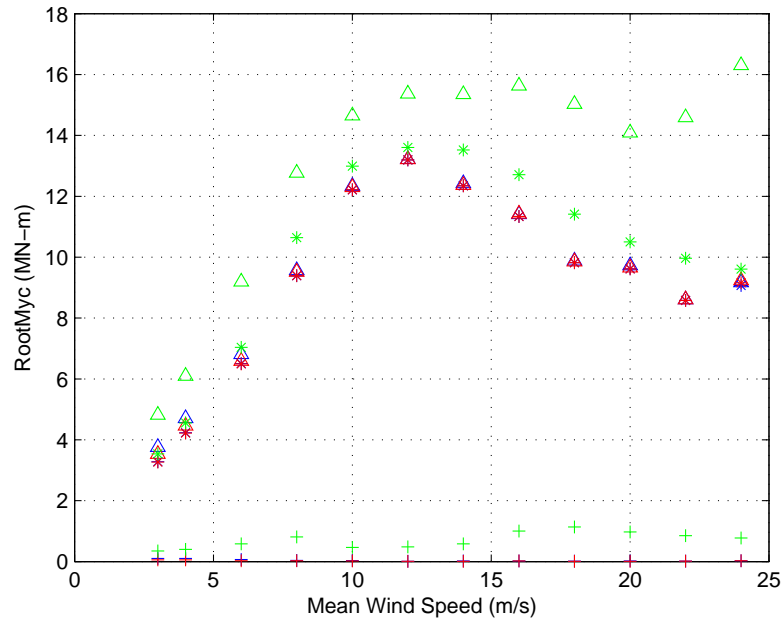


(a) Earthquake Bin: M1R3

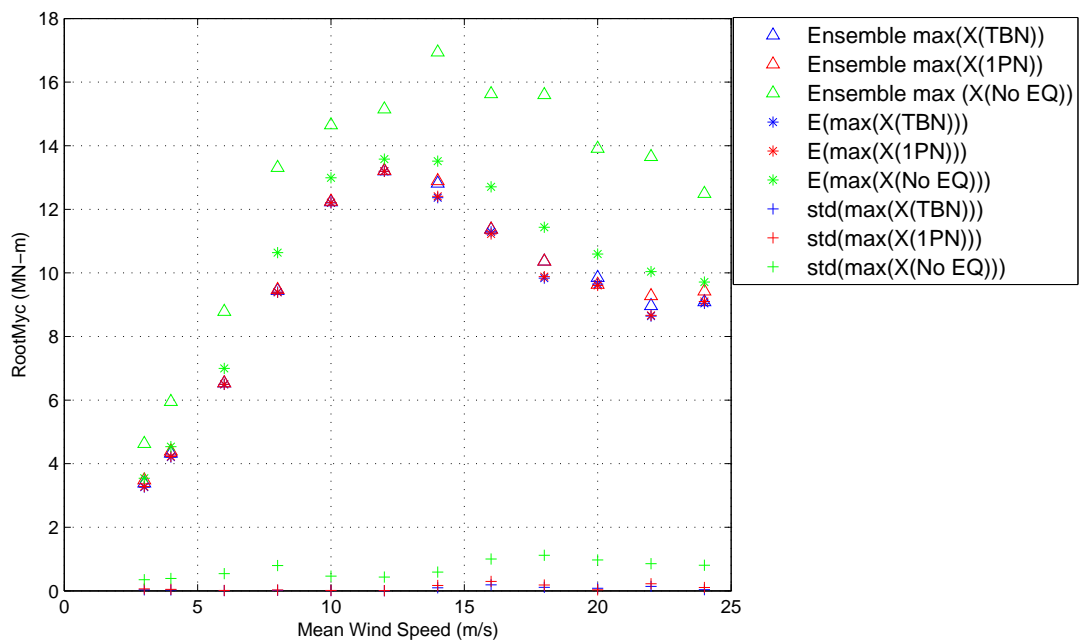
Figure 3.7: Ensemble statistics of blade root out-of-plane bending moment extremes for ground motions belonging to different ground motion bins: (a) M1R1, (b) M1R2, and (c) M1R3, and for varying mean wind speeds at hub height.



(a) Earthquake Bin: M2R1



(b) Earthquake Bin: M2R2



(a) Earthquake Bin: M2R3

Figure 3.8: Ensemble statistics of blade root out-of-plane bending moment extremes for ground motions belonging to different ground motion bins: (a) M2R1, (b) M2R2, and (c) M2R3, and for varying mean wind speeds at hub height.

significantly with ground motion bin (i.e.,  $M$  and  $R$  for the ground motion bin). As was seen when studying time series for the blade root out-of-plane moment, this load process sees a relatively small influence of the ground motion input.

The ten-minute load extremes for the blade root out-of-plane bending moment occur at a mean wind speed close to the rated wind speed—i.e., at either 10 m/s or 12 m/s. Beyond a mean wind speed of 12 m/s, a reduction in the ten-minute load extremes is observed. For the M1R1 bin, the ensemble maximum (overall) of the blade root out-of-plane bending moment is estimated to be 14.6 MN-m and 15.0 MN-m, respectively, for the TBN and 1PN cases. For the same bin, the ensemble maximum based on simulations with the same 3-D turbulent wind fields but with no earthquake input is estimated to be 15.5 MN-m. Thus, unlike the situation with tower loads, very little influence on extremes of the blade root out-of-plane moment is seen when comparing results for the different ground motion bins; this is because the seismic input affects this blade load very slightly compared the aerodynamic loading.

Irrespective of the mean wind speed at hub height and the ground motion input, extremely low standard deviation estimates of load extremes are estimated. The variation in the input energy from the different ground motions considered has very little effect on the extreme blade root moment. This is also the reason why the overall maxima and the mean extreme load levels differ very slightly. The dispersion in load extremes is slightly higher for near-field high-magnitude ground motions and for the lowest mean wind speeds (close to cut-in) when the earthquake input is more important due to the relatively low aerodynamic forces at these low wind speeds.

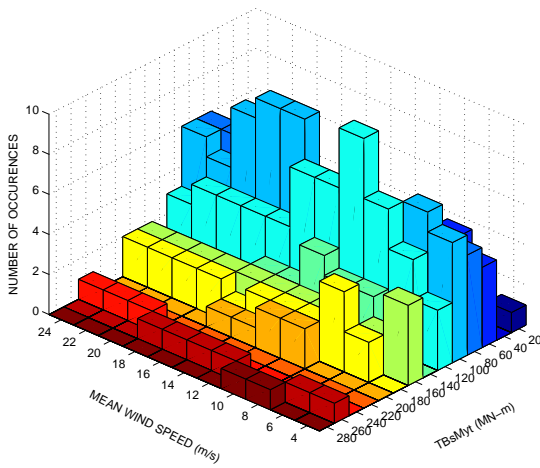
### 3.3.3 Distribution of Response Extremes

In the previous section, ensemble statistics of load extremes were discussed for the different ground motions studied. In this section, the distributions of the turbine load extremes based on fifteen ten-minute simulations for the twenty-five scaled ground acceleration records in each bin and at twelve different hub-height mean wind speeds are discussed in further detail. This section also seeks to explain the relative contributions of wind and earthquake to the response extremes.

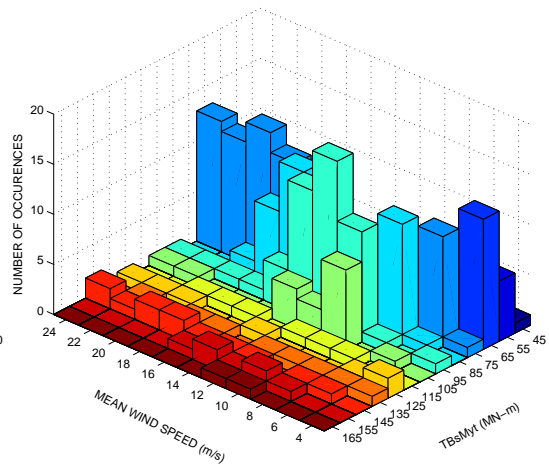
#### 3.3.3.1 Tower Base Fore-Aft Bending Moment

Figure 3.9 presents the distribution of extremes of the tower base fore-aft bending moment for the M1R1 ground motion bin and for different hub-height mean wind speeds. For this  $M$ - $R$  bin, the probability that the tower fore-aft moment exceeds, say, 150 MN-m increases as the mean wind speed approaches the rated wind speed. Further increase in the mean wind speed causes a decrease in the probability of exceedance of large loads. Similar results are observed for the tower fore-aft bending moment extremes for the M1R2, M2R1, and M2R2 bins as presented in Figures 3.10, 3.11, and 3.12, respectively. These distributions show that the response extremes decrease as  $M$  decreases and  $R$  increases.

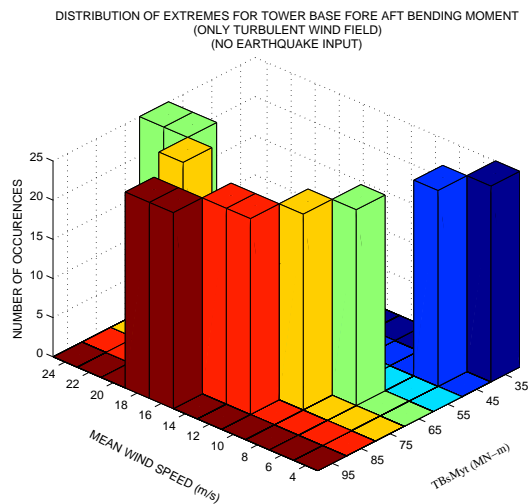
Next, we discuss the relative contributions of the wind and earthquake inputs to the load extremes. In contrast with the distribution of extremes of the tower base fore-aft moment for different ground motions, distributions of this extreme tower load in the absence of ground acceleration rises only up to about 95 MN-m. The extreme load distributions for different ground motion



(a) 1P frequency normalization

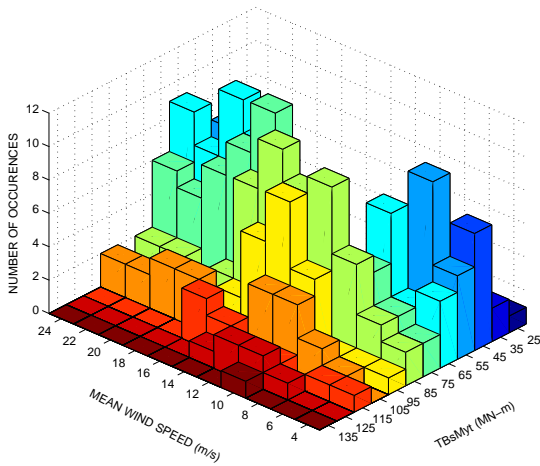


(b) Tower base fore-aft natural frequency normalization

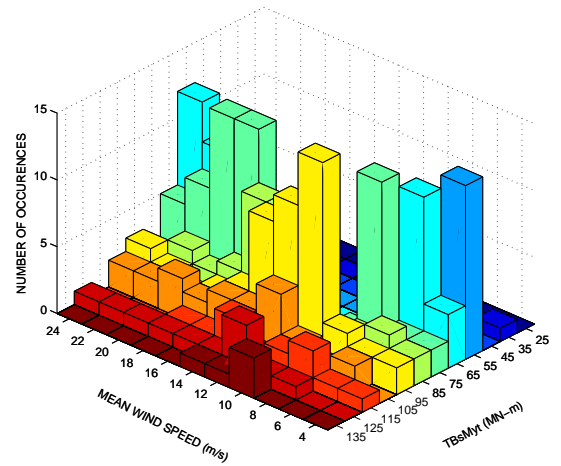


(c) No Earthquake input

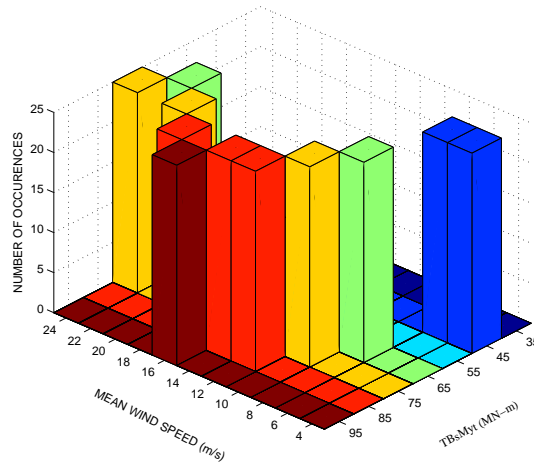
Figure 3.9: Distribution of extremes of the tower base fore-aft bending moment for the M1R1 ground motion bin for: (a) 1P frequency normalization; (b) tower fore-aft bending first-mode frequency normalization; and (c) cases with no earthquake input.



(a) 1P frequency normalization

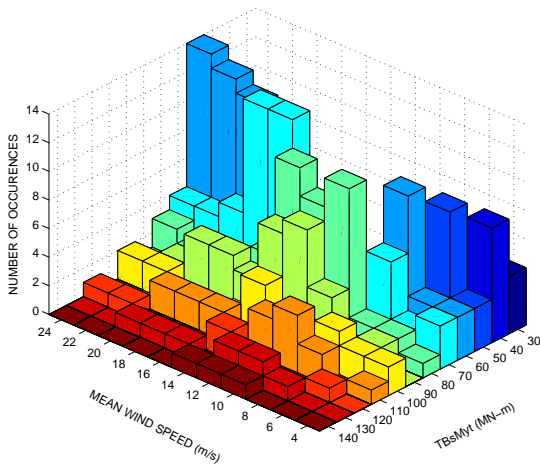


(b) Tower base fore-aft natural frequency normalization

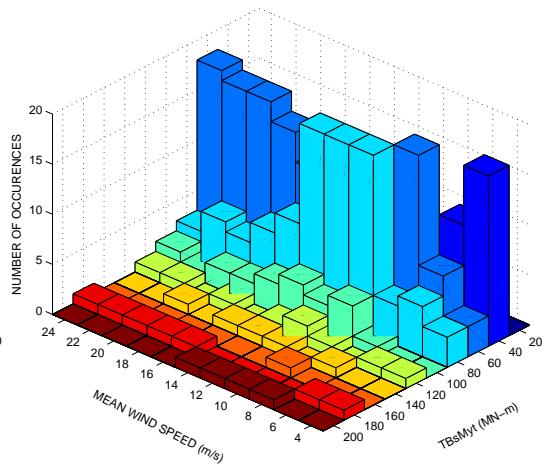


(c) No Earthquake input

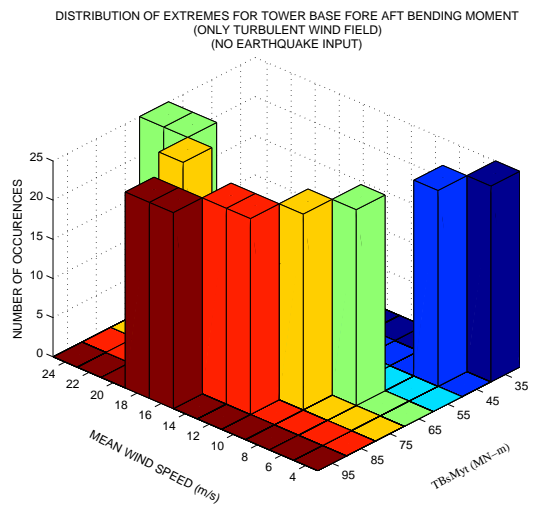
Figure 3.10: Distribution of extremes of the tower base fore-aft bending moment for the M1R2 ground motion bin for: (a) 1P frequency normalization; (b) tower fore-aft bending first-mode frequency normalization; and (c) cases with no earthquake input.



(a) 1P frequency normalization

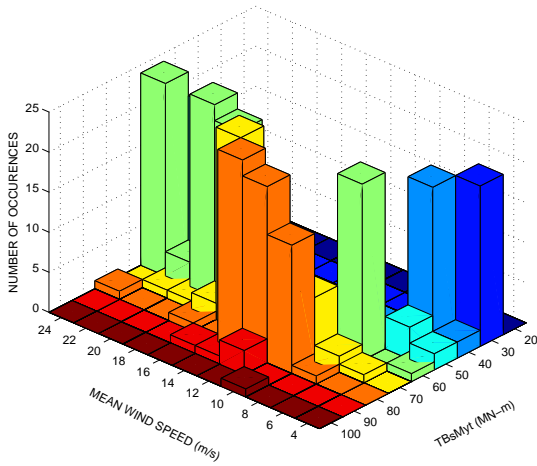


(b) Tower base fore-aft natural frequency normalization

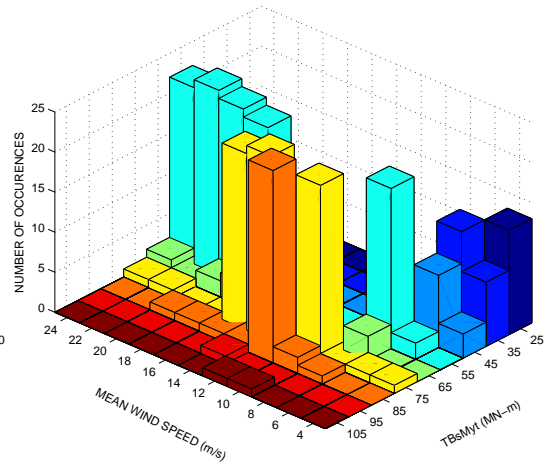


(c) No Earthquake input

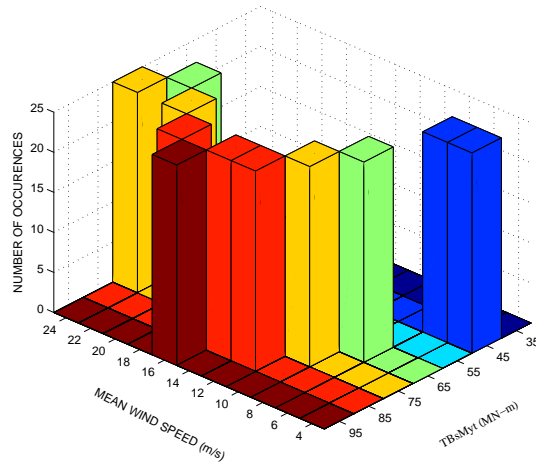
Figure 3.11: Distribution of extremes of the tower base fore-aft bending moment for the M2R1 ground motion bin for: (a) 1P frequency normalization; (b) tower fore-aft bending first-mode frequency normalization; and (c) cases with no earthquake input.



(a) 1P frequency normalization



(b) Tower base fore-aft natural frequency normalization



(c) No Earthquake input

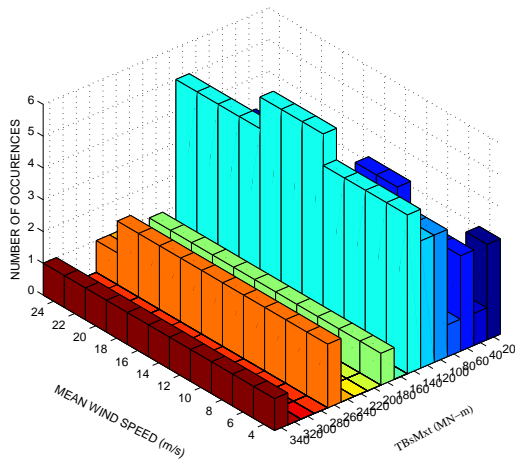
Figure 3.12: Distribution of extremes of the tower base fore-aft bending moment for the M2R2 ground motion bin for: (a) 1P frequency normalization; (b) tower fore-aft bending first-mode frequency normalization; and (c) cases with no earthquake input.

bins show significant variability at a given mean wind speed, whereas those for cases with wind input only describe extreme moments that occur with very low variability. As described by the time series data on loads (Figures 3.1 and 3.2), the tower base fore-aft bending moment extremes is directly related to the onset of the ground acceleration. Thus, the ground acceleration input directly affects the extreme fore-aft bending moment and also contributes to significant variability in the distribution of these load extremes.

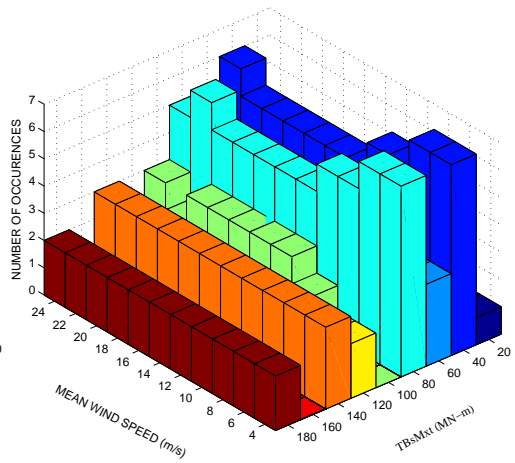
### 3.3.3.2 Tower Base Side-to-Side Bending Moment

Figure 3.13 presents the distribution of extremes of the tower base side-to-side bending moment for the M1R1 ground motion bin and for different hub-height mean wind speeds. A significant increase in the extremes of this load measure are observed for simulations ground motion input compared to cases without any ground motion. Figure 3.13c shows that the extreme tower base side-to-side bending moment caused by the turbulent wind field alone increases monotonically from about 5 MN-m to 35 MN-m as the hub-height mean wind speed increases from the cut-in wind speed (3 m/s) to the cut-out wind speed (25 m/s). In contrast, the variation in extreme load levels is significantly higher in the presence of seismic input and the load distributions are not sensitive to the mean wind speed at all for this M1R1 bin. The input energy at high frequencies from the seismic input and the associated ground accelerations dominates the overall response relative to the relatively less important aerodynamic loads.

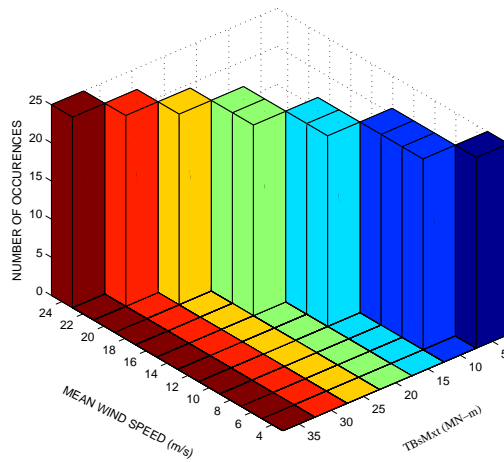
Similar results are also obtained for the distribution of the extreme tower base side-to-side moment for the M1R2, M2R1 and M2R2 bins,



(a) 1P frequency normalization

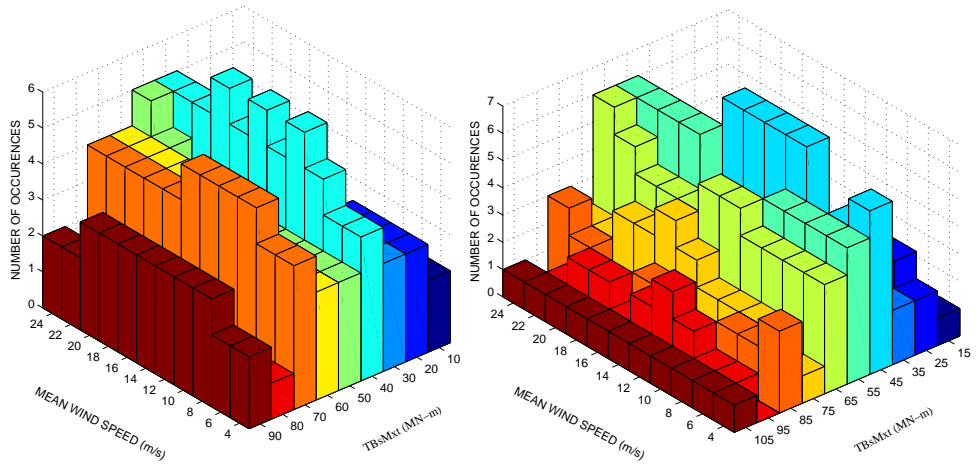


(b) Tower base fore-aft natural frequency normalization

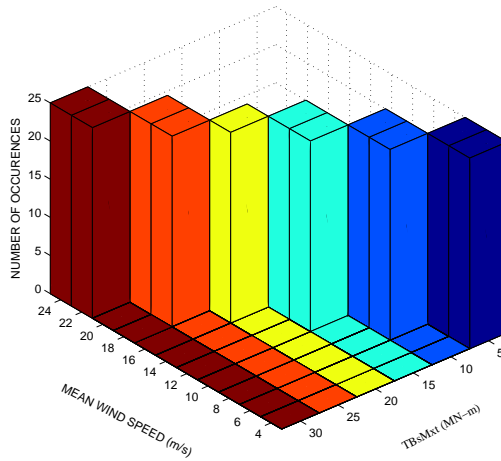


(c) No Earthquake input

Figure 3.13: Distribution of extremes of the tower base side-to-side bending moment for the M1R1 ground motion bin for: (a) frequency normalization; (b) tower fore-aft bending first-mode frequency normalization; and (c) cases with no earthquake input.

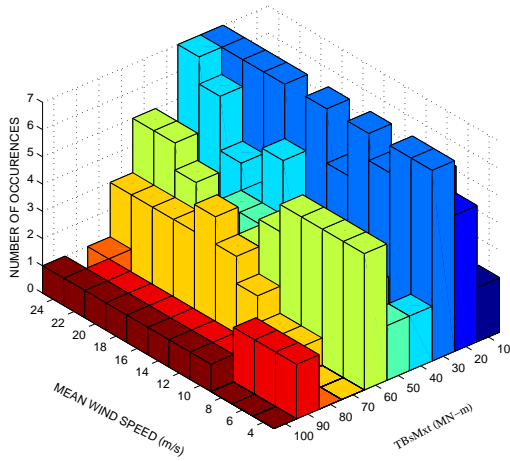


(a) 1P frequency normalization      (b) Tower base fore-aft natural frequency normalization

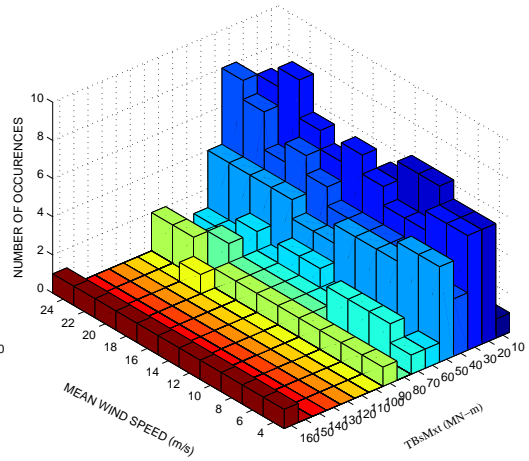


(c) No Earthquake input

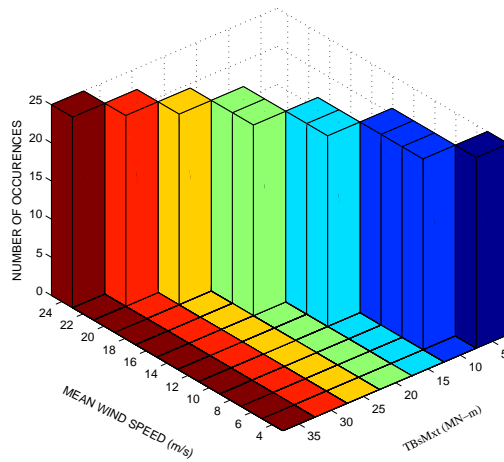
Figure 3.14: Distribution of extremes of the tower base side-to-side bending moment for the M1R2 ground motion bin for: (a) frequency normalization; (b) tower fore-aft bending first-mode frequency normalization; and (c) cases with no earthquake input.



(a) 1P frequency normalization

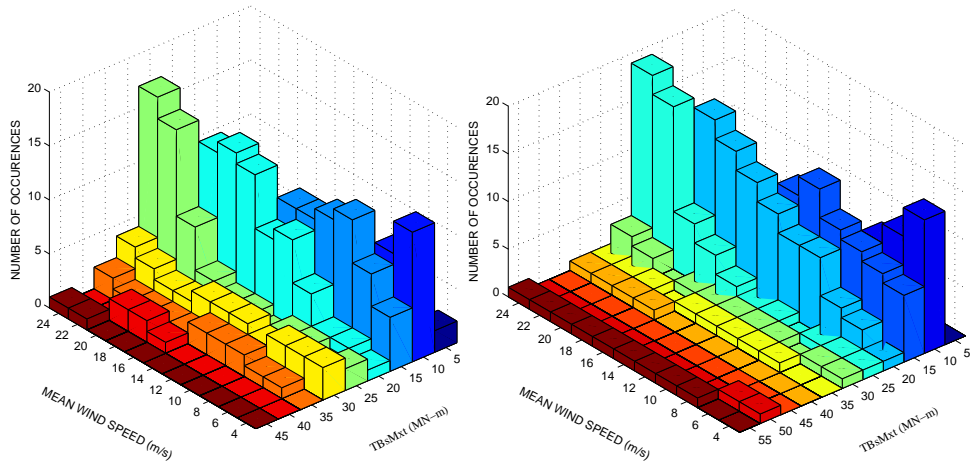


(b) Tower base fore-aft natural frequency normalization

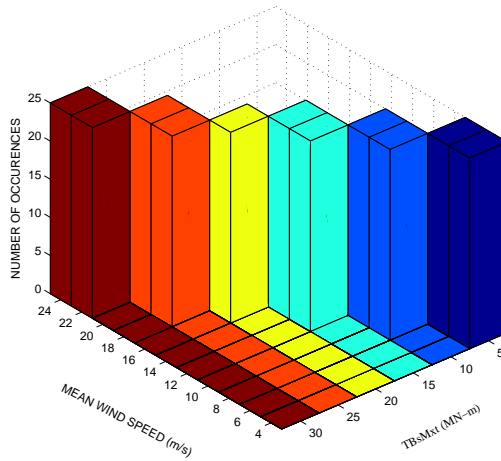


(c) No Earthquake input

Figure 3.15: Distribution of extremes of the tower base side-to-side bending moment for the M2R1 ground motion bin for: (a) frequency normalization; (b) tower fore-aft bending first-mode frequency normalization; and (c) cases with no earthquake input.



(a) 1P frequency normalization      (b) Tower base fore-aft natural frequency normalization



(c) No Earthquake input

Figure 3.16: Distribution of extremes of the tower base side-to-side bending moment for the M2R2 ground motion bin for: (a) frequency normalization; (b) tower fore-aft bending first-mode frequency normalization; and (c) cases with no earthquake input.

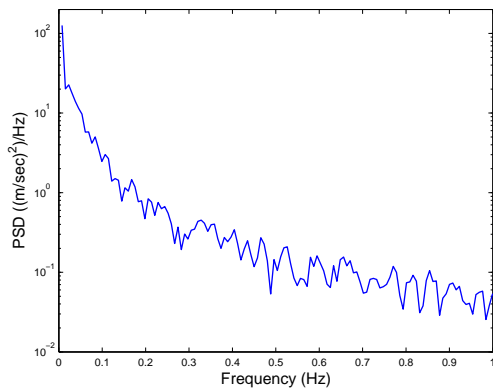
as presented in Figures 3.14, 3.15, and 3.16, respectively. While the load distributions are relatively more sensitive to the mean wind speed (compared to the case with the M1R1 bin) in that larger wind speeds cause larger loads, the primary influence on extreme loads is again predominantly influenced by the seismic input, not by the wind input. Similar to the case with the tower base fore-aft bending moment, the distributions of the extreme tower base side-to-side moment suggest a decrease in extreme values with a decrease in  $M$  and an increase in  $R$ . Largest extreme loads are observed for the near-field large-magnitude ground motions.

### 3.3.4 Power Spectral Density Functions

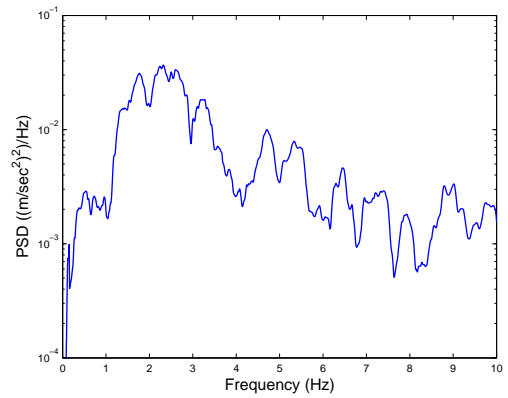
Figure 3.17 presents power spectral density function plots for the simulated hub-height longitudinal wind speed, the scaled ground acceleration in the longitudinal direction, the blade root out-of-plane moment, and the tower base fore-aft moment for a hub-height ten-minute mean wind speed of 10 m/s and ground acceleration input with  $M = 6.9$  and  $R = 13.0$  km (with ground motions scaled to 0.1g in the TBN case). For the same ten-minute mean wind speed and scaled ground acceleration input, Figure 3.18 presents the power spectral density function plots for the simulated hub-height longitudinal wind speed, the scaled ground acceleration component in the transverse direction, the blade root in-plane moment, and the tower base side-to-side moment. The low-frequency energy input from the turbulent wind field has definite but varying effects on the blade and tower response parameters. For the specific simulation discussed here (in Figures 3.17 and 3.18), the energy from the ground acceleration input is concentrated around frequencies ranging

from 2 Hz to 6 Hz, which are considerably higher than the lower frequencies associated with the dominant energy in the turbulent wind field and also higher than the important natural frequencies of vibration of turbine components [18]. The effectiveness of dynamic coupling of the seismic and wind inputs as well as turbine system resonances is evident in the energy evident at both low and high frequencies for various response parameters—for instance, the blade root bending moments and the tower base bending moments exhibit considerable amounts of energy at the lower system natural frequencies even in the presence of seismic input.

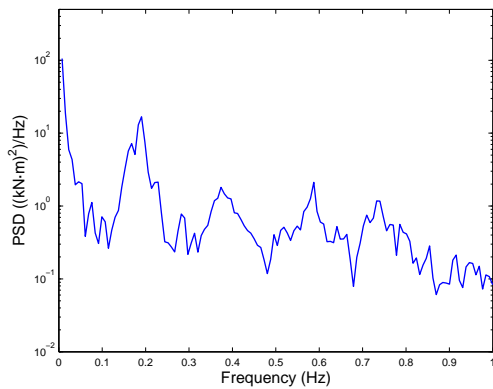
Figures 3.19 to 3.22 present variations in power spectral density functions of various turbine response parameters for simulations involving four different ground acceleration records (from the M1R1 ground motion bin) for hub-height mean wind speeds of 10 m/s and 12 m/s. The blade and tower response parameters show very little variation in the dominant frequencies of the power spectra at the two wind speeds. Somewhat greater variation is seen in the tower loads than in the blade loads as the different ground motions are considered, especially at higher frequencies. The low-frequency energy contribution from the turbulent wind field is evident at both the wind speeds and for all the ground motions. Important peaks in the power spectra for the blade response are observed at the 1P frequency (corresponding to the rotor rotation rate—i.e., 0.2 Hz at and above the rated wind speed) and at multiples of this frequency. The tower base power spectra show peaks around the tower base first-mode natural frequency of vibration (approximately, 0.32 Hz).



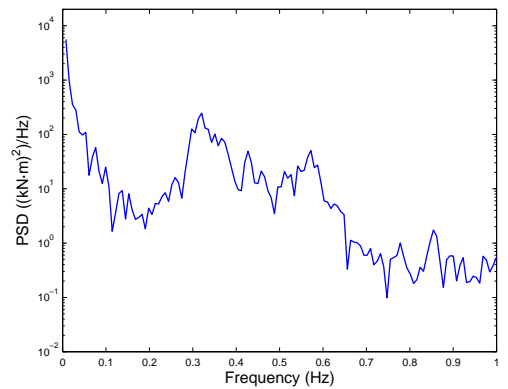
(a) Longitudinal Wind



(b) Longitudinal Ground Acceleration

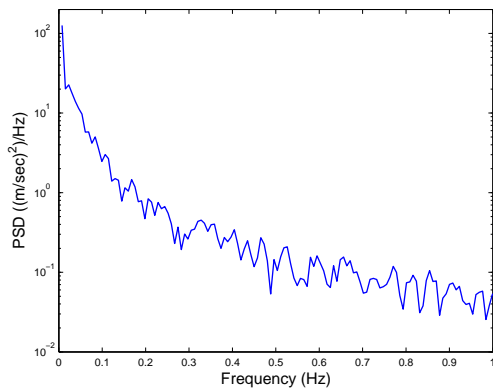


(c) Blade Out-of-Plane Moment

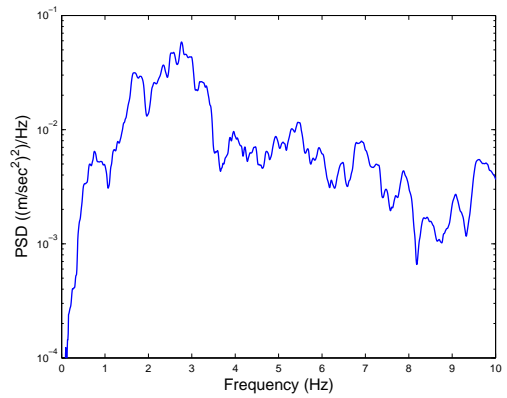


(d) Tower Fore-Aft Moment

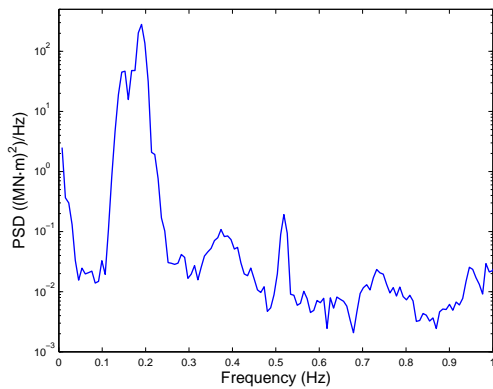
Figure 3.17: Power spectral density functions of the hub-height longitudinal wind speed, the ground acceleration in the longitudinal direction, the blade root out-of-plane moment, and the tower base fore-aft moment for a hub-height longitudinal mean wind speed,  $V_w$ , equal to 10 m/s and ground motion input where  $M = 6.9$  and  $R = 13.0$  km.



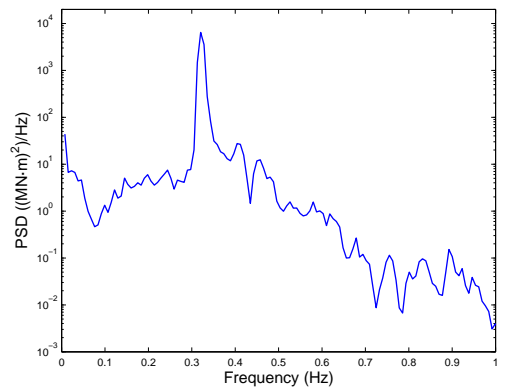
(a) Longitudinal Wind



(b) Transverse Ground Acceleration



(c) Blade In-Plane Moment



(d) Tower Side-to-Side Moment

Figure 3.18: Power spectral density functions of the hub-height longitudinal wind speed, the ground acceleration in the transverse direction, the blade root in-plane moment, and the tower base side-to-side moment for a hub-height longitudinal mean wind speed,  $V_w$ , equal to 10 m/s and ground motion input where  $M = 6.9$  and  $R = 13.0$  km.

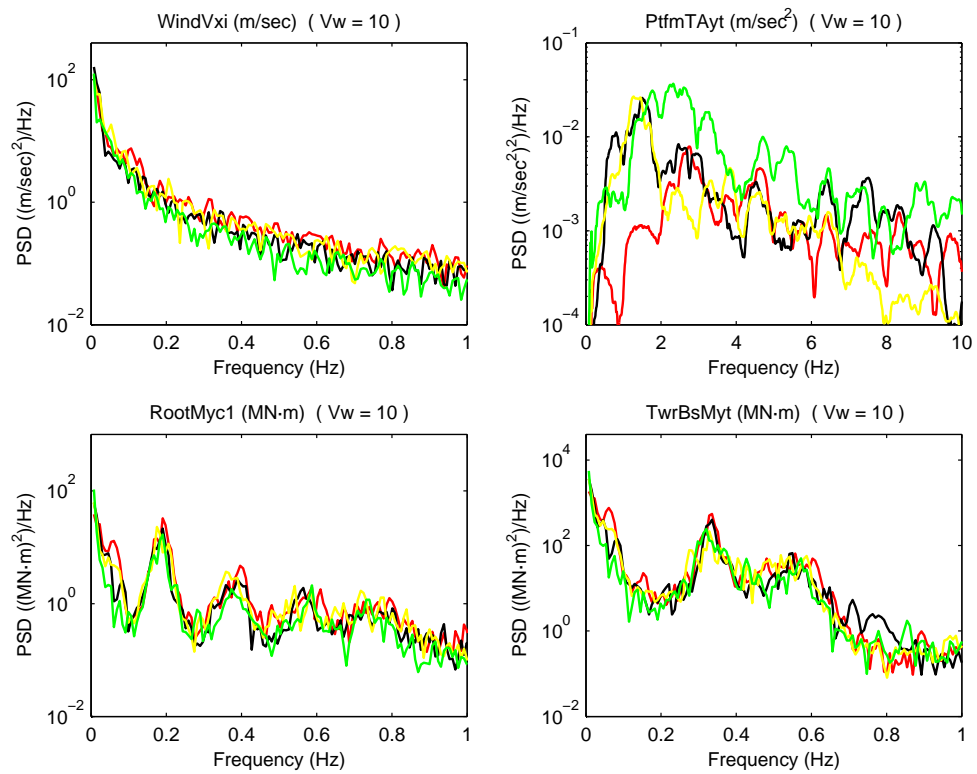


Figure 3.19: Power spectral density functions of the hub-height longitudinal wind speed, the ground acceleration in the longitudinal direction, the blade root out-of-plane moment, and the tower base fore-aft moment for four different ground motion records from the M1R1 bin and for a hub-height longitudinal mean wind speed,  $V_w$ , equal to 10 m/s.

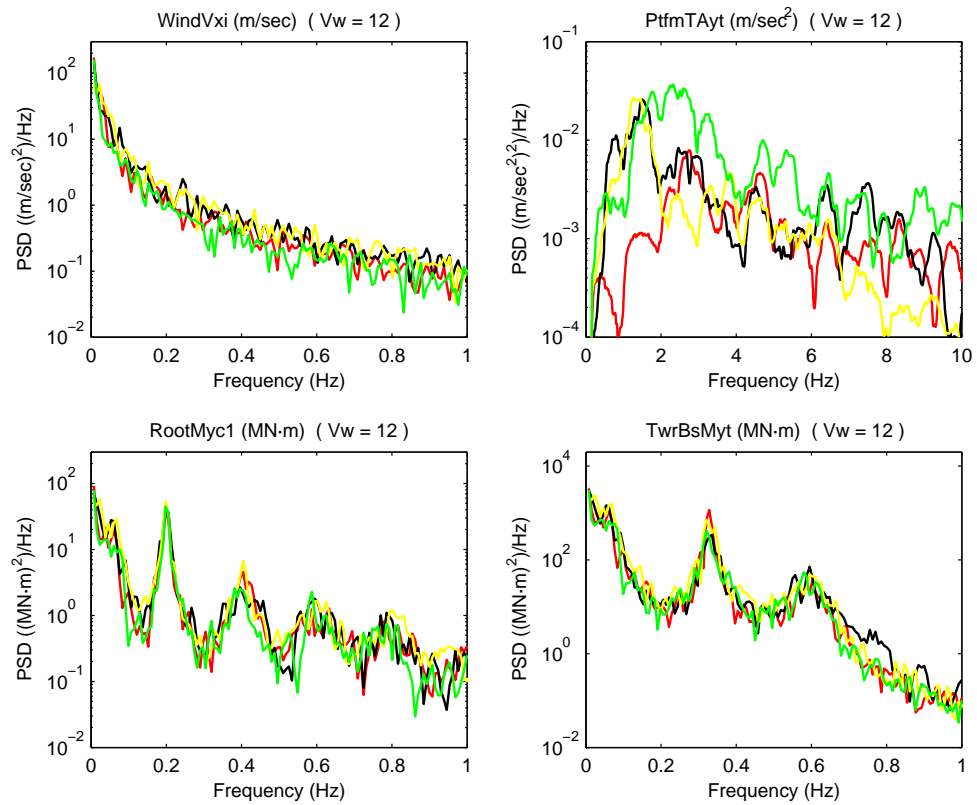


Figure 3.20: Power spectral density functions of the hub-height longitudinal wind speed, the ground acceleration in the longitudinal direction, the blade root out-of-plane moment, and the tower base fore-aft moment for four different ground motion records from the M1R1 bin and for a hub-height longitudinal mean wind speed,  $V_w$ , equal to 12 m/s.

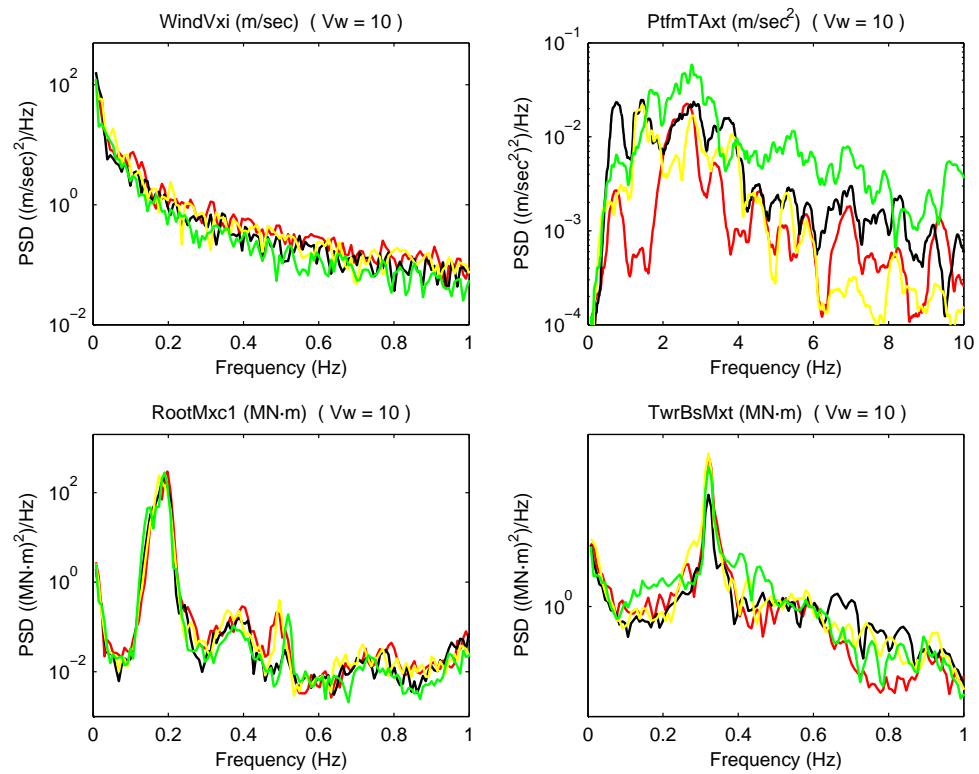


Figure 3.21: Power spectral density functions of the hub-height longitudinal wind speed, the platform acceleration in the transverse direction, the blade root in-plane moment, and the tower base side-to-side moment for four different ground motion records from the MIR1 bin and for a hub-height longitudinal mean wind speed,  $V_w$ , equal to 10 m/s.

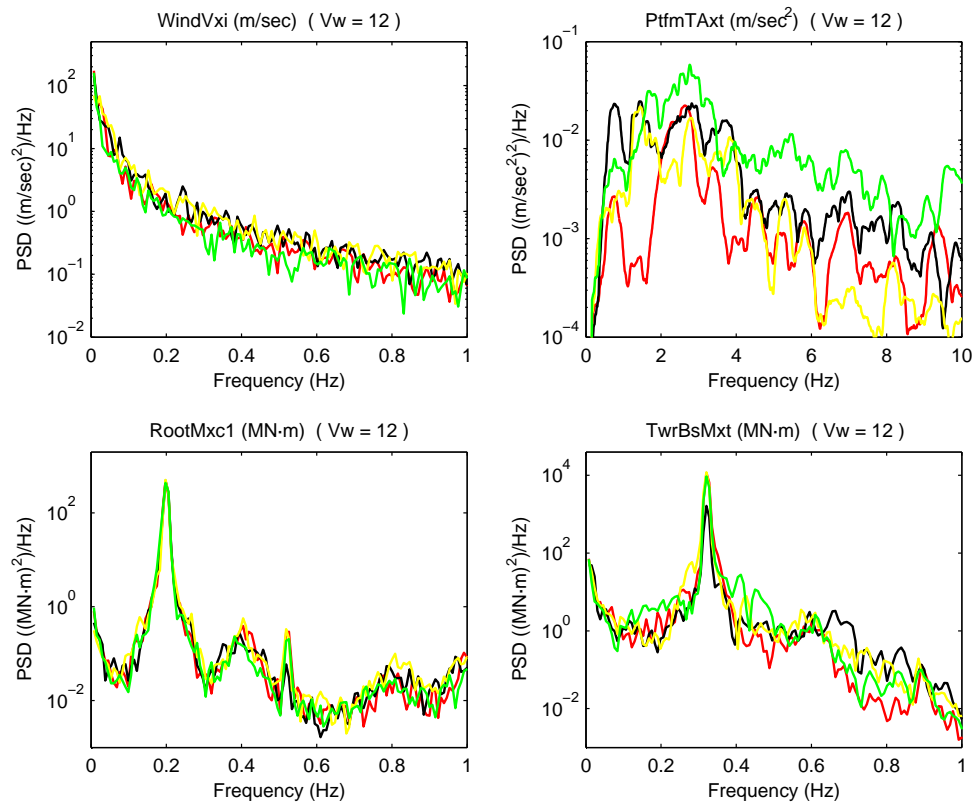


Figure 3.22: Power spectral density functions of the hub-height longitudinal wind speed, the platform acceleration in the transverse direction, the blade root in-plane moment, and the tower base side-to-side moment for four different ground motion records from the M1R1 bin and for a hub-height longitudinal mean wind speed,  $V_w$ , equal to 12 m/s.

### 3.3.5 Interpretation of Turbine Response Statistics

To understand the coupled dynamics of a wind turbine under combined aerodynamic and seismic loads in greater detail, four different FAST simulations were conducted for a single scaled ground acceleration record (for the TBN case) with  $M = 6.9$  and  $R = 13.0$  km and for a mean wind speed of 10 m/s. In each simulation, starting from the 100% scaled earthquake input, the magnitude of the ground acceleration scaling was systematically reduced to 75%, 50%, and 25% of the original scaled record. For comparison purposes, a separate turbine response simulation was carried out without any ground motion input. In all these simulations, the turbulent wind input was kept the same. Results related to the tower base fore-aft bending moment based on this study are discussed next.

Figure 3.23 presents time series of the tower base fore-aft bending moment for the cases with no earthquake input and for 100% earthquake input for the selected ground motion. The maximum tower base fore-aft bending moment for the case with wind input alone is computed to be 70.3 MN-m, which is significantly smaller than the maximum moment of 215.3 MN-m computed for the case with the 100% earthquake input together with the wind input. The time series show dramatic differences in the magnitude and frequency content of the two tower base fore-aft moment response processes. High-frequency energy that results from the interaction of the tower with the input ground motion is evident in the time series for the case that includes the seismic input motion.

Table 3.1 presents a summary of the statistics for the tower base fore-aft bending moment process based on the simulations described above. The mean values of the tower base fore-aft moment show little variation with scal-

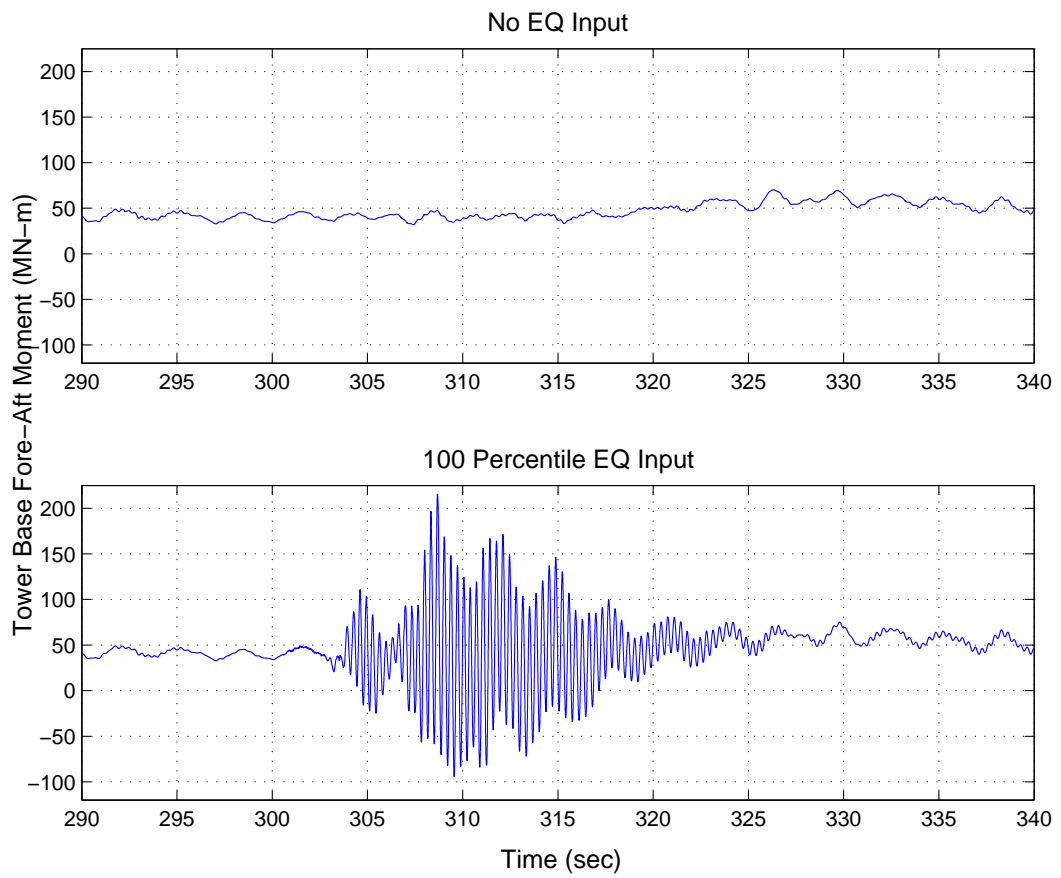


Figure 3.23: Time series (over the period from 290 to 340 seconds) of the tower base fore-aft moment for a hub-height longitudinal mean wind speed,  $V_w$ , equal to 10 m/s, with no seismic input and with a fully 100% scaled seismic input motion for a ground motion bin with  $M = 6.9$  and  $R = 13.0$  km.

Table 3.1: Summary statistics of the tower base fore-aft bending moment process from turbine response simulations with different scaling levels of the seismic input for a ground acceleration records from the ground motion bin with  $M = 6.9$  and  $R = 17.5$  km and for a hub-height mean wind speed,  $V_w$ , equal to 10 m/s.

EQ Scaling	Max (MN-m)	Mean (MN-m)	Std. (MN-m)	Skewness	Kurtosis	Upcrossing Rate ( $s^{-1}$ )	P.F.
No EQ	70.27	48.66	9.06	0.37	2.09	0.23	2.38
25%	89.79	48.66	12.94	0.70	3.57	0.23	3.18
50%	131.81	48.66	20.34	0.72	5.16	0.25	4.08
75%	173.74	48.65	28.61	0.73	5.82	0.29	4.37
100%	215.33	48.64	37.15	0.79	6.11	0.325	4.49

ing of the input ground motion; the mean of this response process depends only on wind input. The standard deviation of the load process induced by ground motion levels with as low as 25% scaling is comparable to the standard deviation of the load based on the wind input alone (for this case where the hub-height mean wind speed is 10 m/s). The high-frequency ground motion input leads to this significant increase in the load process standard deviation even at the lower ground motion scaling levels.

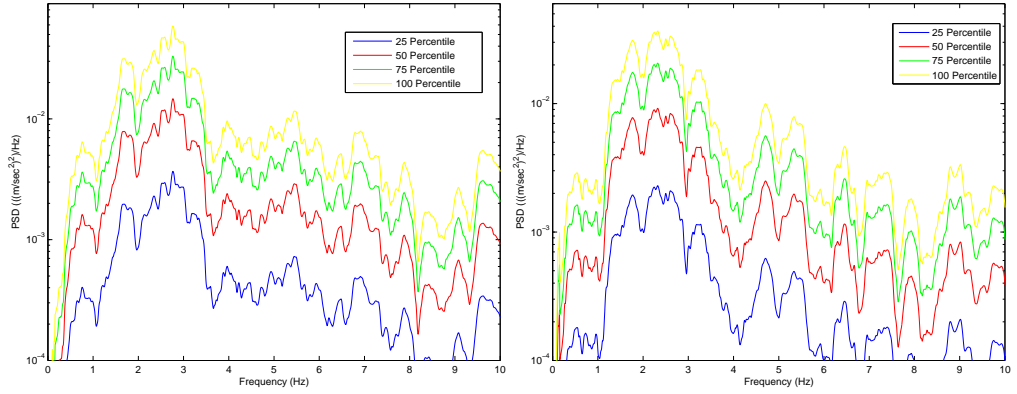
Another statistical parameter, the Peak Factor (P.F.) of the load process provides an indication of how many standard deviations the maximum response is over the mean of the process. A significant increase in the peak factor is noted when going from the wind input only case to the 100%-scaled ground motion case. The peak factor depends on higher-order load statistics such as the process skewness and kurtosis that influence the tails of the load distribution. Increases in skewness and kurtosis estimates play an important part in overall response peak factor amplification. Higher positive skewness

estimates and higher kurtosis estimates move more probability mass to the tails of the load distribution—this leads to larger extremes. Additionally, an increase in the mean upcrossing rate also contributes to peak factor amplification because of a larger number of response cycles that occur in the same duration. In sum, both the amplification of the process peak factor as well as an increase in the process standard deviation leads to a pronounced increase in the tower base fore-aft bending moment extreme from the case without any earthquake input to the case with the 100%-scaled ground motion even though the process mean value remains relatively constant. This amplification of the peak factor and increase in the standard deviation occurs largely due to an increase in the high-frequency content in the tower base fore-aft bending moment process. Figure 3.24 shows power spectral density function plots for the two horizontal ground acceleration components at different scaling levels, the hub-height longitudinal wind velocity, and the tower base fore-aft bending moment for cases with different ground acceleration scaling levels while the hub-height mean wind speed is set at 10 m/s. A high-frequency peak in the power spectra for the tower bending moment that grows with increased seismic input is evident in the plots.

### **3.3.6 Transients and Directionality**

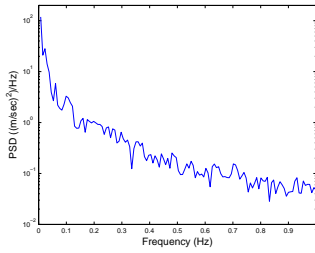
#### **3.3.6.1 Effects of Variation in Pre-earthquake Transient Period**

In preceding sections, it has been observed that extremes of the tower base fore-aft bending moment as well as tower base side-to-side bending moment are governed by the high-frequency energy input from the ground acceleration time series. This duration of high-frequency energy input, however,

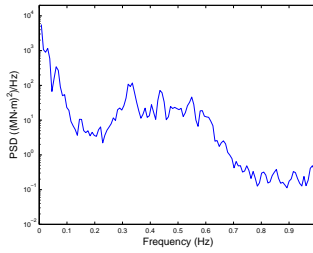


(a) Transverse Ground Acceleration

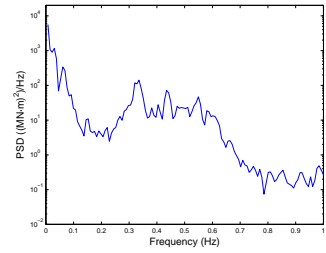
(b) Longitudinal Ground Acceleration



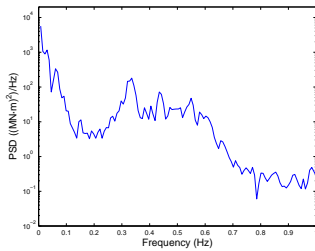
(c) Wind



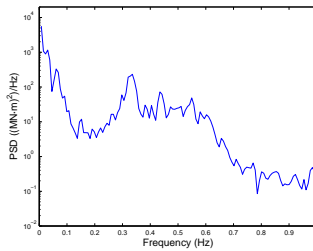
(d) TBsMyt (No EQ input)



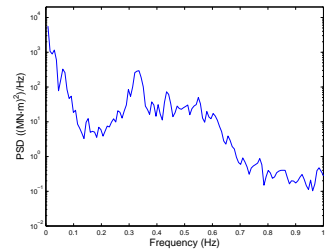
(e) TBsMyt (25 Percentile)



(f) TBsMyt (50 Percentile)



(g) TBsMyt (75 Percentile)



(h) TBsMyt (100 Percentile)

Figure 3.24: Power spectral density functions of the transverse and longitudinal ground acceleration components at different scaling levels [(a),(b)]; the longitudinal wind velocity at hub height [c]; the tower base fore-aft bending moment with no earthquake input [d]; and the tower-base fore-aft bending moment for 25%, 50%, 75%, and 100% scaling [(e), (f), (g), (h)] of a ground acceleration record from a bin with  $M = 6.9$  and  $R = 13$  km and for a hub-height mean ten-minute wind speed,  $V_w$ , equal to 10 m/s.

is generally considerably shorter than the total simulation length—i.e., 600 seconds. In the case of a seismic event, the operational characteristics of the turbine prior to when the ground motion strikes may vary. In order to study the variation in tower response extremes with variation in the initial transient period before the earthquake strikes, ten-minute simulations were run by changing the pre-earthquake transient period from 20 seconds to 100 seconds in increments of 20 seconds. Figure 3.25 shows time series for both fore-aft and side-to-side tower base moments at a mean wind speed of 10 m/s and for a ground acceleration record belonging to the M1R1 bin (where  $M = 6.9$  and  $R = 13.0$  km) with different transient periods prior to the onset of ground shaking.

Table 3.2 describes the variation in extremes of the tower base fore-aft and side-to-side bending moments for the ten-minute simulations with different (transient) durations of pre-earthquake wind input. These load extremes show very little variation with changes in this transient period during which the turbulent wind field is the same and the hub-height mean wind speed is 10 m/s. This is because the occurrence of the tower base moment extremes is dominated by the ground acceleration input rather than by the turbulent wind input.

### **3.3.6.2 Effects of Orientation of Horizontal Ground Motion Components**

In order to assess the influence of the ground acceleration input relative to the inflow wind field on the turbine tower loads, ground motion direction considerations are important. In the present study, among the two horizontal components for each available ground motion record in the database, the

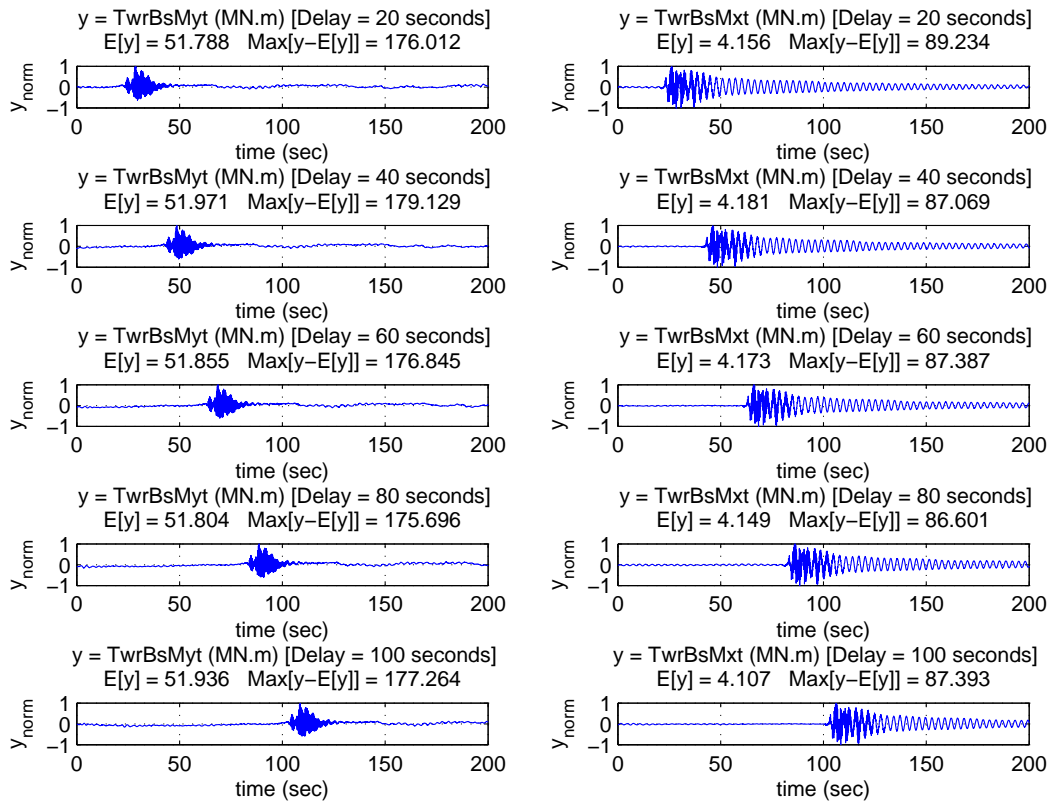


Figure 3.25: Time series (over the period from zero to 200 seconds) of the tower base fore-aft and side-to-side bending moments for a hub-height longitudinal wind speed,  $V_w$ , equal to 10 m/s and for a ground motion record where  $M = 6.9$  and  $R = 13.0$  km with different transient periods prior to ground shaking that vary from 20 to 100 seconds.

Table 3.2: Extremes of the tower base fore-aft (TBsMyt) and side-to-side (TBsMxt) bending moments for varying transient periods for a ground acceleration record where  $M = 6.9$  and  $R = 13.0$  km and for a hub-height ten-minute mean wind speed,  $V_w$ , equal to 10 m/s.

Transient Period (seconds)	Max(TBsMyt) (MN-m)	Max(TBsMxt) (MN-m)
20	227.80	93.39
40	231.10	90.40
60	228.70	91.45
80	227.50	90.75
100	229.20	90.32

Table 3.3: Extremes of the tower base fore-aft (TBsMyt) and side-to-side (TBsMxt) bending moments for varying orientations of the horizontal components of the input ground acceleration with respect to the wind turbine where the ground acceleration record is from a bin where  $M = 6.9$  and  $R = 13.0$  km and the hub-height ten-minute mean wind speed,  $V_w$ , is equal to 10 m/s.

Orientation Angle (seconds)	Max(TBsMyt) (MN-m)	Max(TBsMxt) (MN-m)
$0^\circ$	215.11	90.86
$15^\circ$	207.73	94.29
$30^\circ$	192.63	112.95
$45^\circ$	172.51	136.12
$60^\circ$	150.65	150.74
$75^\circ$	132.82	158.95
$90^\circ$	135.21	168.36

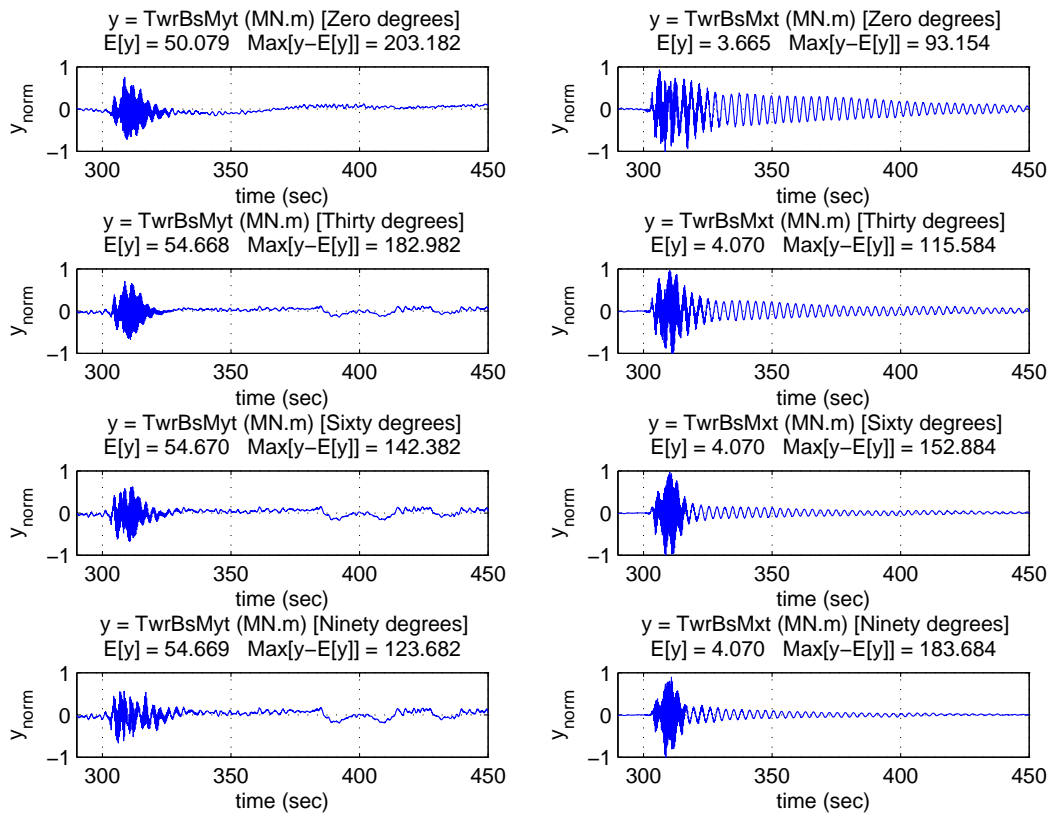


Figure 3.26: Time series (over the period from 290 to 450 seconds) of the tower base fore-aft and side-to-side bending moment for a hub-height longitudinal wind speed,  $V_w$ , equal to 10 m/s, and for a ground motion record where  $M = 6.9$  and  $R = 13.0$  km for alternate orientations of the horizontal components of the input ground acceleration with respect to the wind turbine.

one with the higher peak ground acceleration was systematically employed in the longitudinal direction and was, as such, aligned with the direction of the non-zero mean speed. Due to the possibility of random orientation, in general, of the turbine rotor plane relative to the input ground motion, the component with the higher peak ground acceleration may not be aligned with the direction of the (longitudinal) wind direction. To assess ground motion orientation considerations, ten-minute turbine response simulations were conducted for the same ground motion records but with the orientation of the horizontal components systematically rotated by fifteen degrees to examine various situations. Figure 3.26 shows time series for the tower base fore-aft and side-to-side bending moments for a ground motion records from the M1R1 bin (where  $M = 6.9$  and  $R = 13.0$  km) and for a hub-height mean wind speed of 10 m/s. In the figure, the ‘Zero Degrees’ case corresponds to the orientation where the horizontal component of ground acceleration with the higher peak ground acceleration (PGA) is aligned with the longitudinal inflow wind field direction (and the non-zero mean wind direction) while the ‘Ninety Degrees’ case corresponds to the orientation where the horizontal component of ground acceleration with the lower PGA is aligned with the longitudinal wind direction.

Table 3.3 shows the variation of the extreme tower loads for alternate orientations of the horizontal components of the ground acceleration record while the hub-height mean wind speed is set at 10 m/s. The extreme tower base fore-aft bending moment is seen to decrease as the orientation of the horizontal ground motion components is changed from zero to ninety degrees; simultaneously, the extreme tower base side-to-side bending moment is seen to increase. Similar results are observed for mean wind speeds other than 10 m/s. In most cases, the maximum values of the extreme fore-aft moment cor-

respond to the zero-degree orientation. Thus, the results of the present study correspond to the worst-case orientation for the tower base moment in general (i.e., without consideration for side-to-side versus fore-aft bending); the expected extreme tower loads on a turbine for any random earthquake event and rupture path will in general be less than those considered here with the zero-degree orientation assumption.

### **3.4 Summary**

This chapter presented a statistical study of the dynamically coupled response of a wind turbine in the time domain. Results from the turbine simulations for various turbine response parameters were presented in the form of a statistical study of the extremes of tower and blade loads by making use of time series and power spectra. Turbine tower base bending loads were studied in greater detail by considering variations in the amount of scaled seismic input introduced in the ground motion records. Turbine tower base bending loads displayed significant energy at low frequencies driven by wind input; however, extremes of these loads were larger for near-field high-magnitude ground motion records where the seismic input energy was high. Unlike the tower response, turbine blade response extremes showed very slight influence of the input seismic energy. Both tower and blade loads were largest for wind speeds close to turbine's rated wind speed. Aeroelastic damping effects appeared to play a significant in turbine blade and tower response. The effect of pre-earthquake transients on turbine tower loads was found to be very slight. Alternative orientation of the horizontal ground motion components were found to influence turbine tower loads; in general, orienting the horizontal compo-

ment of the ground acceleration with the larger peak ground acceleration with the direction of the longitudinal wind resulted in the largest overall tower base bending moment.

## Chapter 4

### Conclusions

#### 4.1 Outline of Research Conducted

Seismic demand on wind turbines has not been given much attention in turbine loads analysis, even in seismically active regions. Some turbine design standards and industry guidelines address issues related to the seismic design of wind turbines. However, they provide a very generalized view on the methods for such seismic analysis. Various simplified and full-system wind turbine models have been published and used for seismic analyses of turbine loads in recent times. This study involved the analysis of extreme loads on the 5-MW NREL baseline wind turbine model during a seismic event based on simulations using the open-source software, FAST. The study attempted to explain the dynamic behavior of the turbine when subjected jointly to aerodynamic as well as seismic loads. By means of time-domain stochastic simulations, estimates of tower and rotor extreme loads were obtained for critical combinations of hub-height mean wind speeds and for several groups of earthquake ground acceleration records.

#### 4.2 Conclusions

A statistical analysis of the extreme loads for the 5-MW NREL baseline wind turbine over the range of operational mean wind speeds at hub height—i.e., from the cut-in wind speed of 3 m/s to the cut-out wind speed of 25

m/s—was carried out for 150 ground acceleration motion records belonging to six different earthquake bins based on the magnitude of the earthquake and the distance of the recording station from the point of rupture. This study attempted to explain the dynamics of the wind turbine under combined aerodynamic and seismic loads using statistical summaries of extreme tower and blade loads. Some important conclusions drawn from this study follow.

- Extremes of the tower base bending moment are significantly affected by the seismic ground acceleration input. The distribution of the extremes of the tower base fore-aft as well as side-to-side bending moments suggest that when seismic ground acceleration is included in turbine loads analyses during normal operation, tower base bending moments are significantly higher than those during normal operation with only turbulent wind input.
- The maximum tower loads for a given ground motion bin are observed to occur at a mean wind speed at hub height close to the rated wind speed. Extreme tower loads at a given wind speed increase with an increase in the magnitude of the earthquake to which the ground acceleration record is associated. Also, these extremes decrease with an increase in distance from the fault rupture.
- The orientation of the ground acceleration records with respect to the wind turbine plays an important role in determining extreme tower loads. This study suggests that the maximum tower loads generally occur when, among the two horizontal components of ground acceleration, the one with the higher intensity of shaking (or higher peak ground acceleration) is aligned with the longitudinal wind direction (i.e., with the non-zero

mean wind direction). This is due to the mean component of the tower base fore-aft moment that results from the aerodynamic loading. In all other orientations of the horizontal ground acceleration components, the tower base bending loads are generally lower. The present study focused on tower loads during the worst-case orientation scenario.

- Unlike tower loads, blade root bending moments do not show a significant influence of the seismic input. The distribution of the extremes of the blade root in-plane and out-of-plane bending moment suggest little to no dependence on the ground acceleration input.
- The variation in the transient wind-only period before any ground acceleration does not affect the extreme values of turbine tower loads. The extremes of the tower loads depend less on the turbulent wind input but are greatly influenced by the ground acceleration input.
- Time series and power spectral density functions for the tower base response parameters show contributions from frequencies associated with seismic input as well as low-frequency energy from the turbulent wind field; resonant frequencies associated with tower bending are clearly influenced by the level of seismic input.

### **4.3 Future Research Prospects**

The above conclusions are presented with an intention that they may be used by wind turbine designers for estimating extreme loads on a wind turbine located in a region of moderate to high seismic activity. These results, as explained in the previous chapters, are based on an extensive study

organized by simulating various earthquake records from Western U.S. earthquakes. For the purpose of comparative studies, these earthquake records were normalized using spectral acceleration at two different frequencies of interest in turbine dynamics—i.e., the 1P frequency of rotor rotation and the tower base first fore-aft mode frequency. The normalization process played a crucial role in determining extreme loads. Similar studies with the earthquake records normalized to spectral acceleration at frequencies corresponding to higher modes of turbine vibration may be executed for studying the coupled dynamics of the seismic and aerodynamic loads in greater detail. However, the normalization process must be executed with extreme care so as not to lose inherent and realistic characteristics of the records.

As discussed, the orientation of the earthquake ground acceleration record with respect to the rotor plane of the turbine plays a crucial role in determining the extreme tower loads. In this study, that horizontal component (of two) of ground acceleration with the higher peak ground acceleration was aligned with the direction of the longitudinal wind speed for all the turbine response simulations. For most records, this orientation provided the worst-case scenario as far as tower base loads are concerned. However, due to the random nature of possible alternate combined seismic and wind input, the probability of the occurrence of this worst-case scenario is small. Hence, detailed ground motion orientation studies (relative to ambient winds) are important to obtain more realistic estimates of the extreme turbine loads for random seismic inputs.

Findings from studies such as this one as well as subsequent studies that might expand on results presented here can be useful in giving wind turbine designers increased confidence in wind turbine design for extreme seismic loading and can, thus, lead to safer designs.

## Appendix

## Appendix A

### List of Ground Acceleration Records

Table A.1: List of earthquake records used for ten-minute FAST simulations for the earthquake bin M1R1.

Earthquake	PEER Record Number	Moment Magnitude	Distance from Fault Rupture (km)
1992, Cape mendocino	P0806	7.1	8.5
1971, San Fernando	P0082	6.6	2.8
1992, Cape mendocino	P0809	7.1	9.5
1992, Landers	P0873	7.3	1.1
1989, Loma Prieta	P0733	6.9	11.2
1989, Loma Prieta	P0736	6.9	14.4
1989, Loma Prieta	P0737	6.9	16.1
1989, Loma Prieta	P0744	6.9	14.5
1989, Loma Prieta	P0745	6.9	5.1
1989, Loma Prieta	P0760	6.9	10.3
1989, Loma Prieta	P0764	6.9	11.6
1989, Loma Prieta	P0770	6.9	6.1
1989, Loma Prieta	P0779	6.9	13.0
1994, Northridge	P0887	6.7	9.2
1994, Northridge	P0890	6.7	19.6
1994, Northridge	P0893	6.7	13.0
1994, Northridge	P0928	6.7	8.2
1994, Northridge	P0934	6.7	6.4
1994, Northridge	P0963	6.7	6.2
1994, Northridge	P0964	6.7	2.6
1994, Northridge	P0995	6.7	8.0
1994, Northridge	P1005	6.7	7.1
1994, Northridge	P1020	6.7	8.9

1994, Northridge	P1023	6.7	6.2
1994, Northridge	P1024	6.7	6.1

Table A.2: List of earthquake records used for ten-minute FAST simulations for the earthquake bin M1R2.

Earthquake	PEER Record Number	Moment Magnitude	Distance from Fault Rupture
1992, Landers	P0814	7.3	23.2
1992, Landers	P0818	7.3	24.2
1992, Landers	P0865	7.3	21.2
1989, Loma Prieta	P0734	6.9	21.8
1989, Loma Prieta	P0743	6.9	21.4
1989, Loma Prieta	P0747	6.9	25.8
1989, Loma Prieta	P0761	6.9	22.3
1989, Loma Prieta	P0769	6.9	28.8
1989, Loma Prieta	P0773	6.9	36.1
1989, Loma Prieta	P0774	6.9	36.3
1989, Loma Prieta	P0789	6.9	28.8
1994, Northridge	P0883	6.7	22.6
1994, Northridge	P0889	6.7	20.8
1994, Northridge	P0903	6.7	31.3
1994, Northridge	P0904	6.7	30.9
1994, Northridge	P0905	6.7	25.7
1994, Northridge	P0910	6.7	23.9
1994, Northridge	P0914	6.7	30.0
1994, Northridge	P0921	6.7	38.3
1994, Northridge	P0925	6.7	28.0
1994, Northridge	P0937	6.7	24.2
1994, Northridge	P0941	6.7	32.4
1994, Northridge	P0962	6.7	25.7
1994, Northridge	P1017	6.7	27.6
1994, Northridge	P1022	6.7	22.2

Table A.3: List of earthquake records used for ten-minute FAST simulations for the earthquake bin M1R3.

Earthquake	PEER Record Number	Moment Magnitude	Distance from Fault Rupture
1989, Loma Prieta	P0740	6.9	43.0
1989, Loma Prieta	P0753	6.9	47.9
1989, Loma Prieta	P0754	6.9	57.4
1989, Loma Prieta	P0756	6.9	46.9
1989, Loma Prieta	P0762	6.9	51.2
1989, Loma Prieta	P0763	6.9	43.4
1989, Loma Prieta	P0767	6.9	58.9
1994, Northridge	P0888	6.7	46.6
1994, Northridge	P0895	6.7	49.6
1994, Northridge	P0896	6.7	40.7
1994, Northridge	P0897	6.7	47.6
1994, Northridge	P0898	6.7	47.4
1994, Northridge	P0901	6.7	44.7
1994, Northridge	P0902	6.7	41.9
1994, Northridge	P0919	6.7	59.3
1994, Northridge	P0924	6.7	42.0
1994, Northridge	P0936	6.7	60.0
1994, Northridge	P0938	6.7	42.5
1994, Northridge	P0946	6.7	44.2
1994, Northridge	P0947	6.7	50.6
1994, Northridge	P0948	6.7	67.3
1994, Northridge	P1002	6.7	54.3
1994, Northridge	P1007	6.7	46.6
1994, Northridge	P1011	6.7	41.7
1994, Northridge	P1016	6.7	52.5

Table A.4: List of earthquake records used for ten-minute FAST simulations for the earthquake bin M2R1.

Earthquake	PEER Record Number	Moment Magnitude	Distance from Fault Rupture
1986, Chalfant Valley	P0555	6.2	18.7
1979, Coyote Lake	P0146	5.7	9.3
1979, Coyote Lake	P0147	5.7	3.2
1979, Coyote Lake	P0148	5.7	7.5
1979, Coyote Lake	P0149	5.7	6.0
1979, Coyote Lake	P0150	5.7	4.5
1979, Imperial Valley	P0159	6.5	8.5
1979, Imperial Valley	P0160	6.5	12.9
1979, Imperial Valley	P0161	6.5	2.5
1979, Imperial Valley	P0162	6.5	8.5
1979, Imperial Valley	P0163	6.5	10.6
1979, Imperial Valley	P0172	6.5	0.5
1979, Imperial Valley	P0173	6.5	15.5
1979, Imperial Valley	P0175	6.5	9.3
1979, Imperial Valley	P0176	6.5	4.2
1979, Imperial Valley	P0177	6.5	1.0
1984, Morgan Hill	P0454	6.2	3.4
1984, Morgan Hill	P0458	6.2	2.6
1986, N. Palm Springs	P0516	6.0	16.3
1966, Parkfield	P0031	6.1	5.3
1966, Parkfield	P0032	6.1	9.2
1966, Parkfield	P0034	6.1	9.9
1987, Whittier Narrows	P0624	6.0	12.1
1987, Whittier Narrows	P0693	6.0	10.8

Table A.5: List of earthquake records used for ten-minute FAST simulations for the earthquake bin M2R2.

Earthquake	PEER Record Number	Moment Magnitude	Distance from Fault Rupture
1986, Chalfant Valley	P0551	6.2	37.2
1986, Chalfant Valley	P0552	6.2	23.0
1983, Coalinga	P0323	6.4	25.5
1983, Coalinga	P0336	6.4	37.9
1983, Coalinga	P0337	6.4	36.4
1983, Coalinga	P0340	6.4	31.0
1983, Coalinga	P0341	6.4	29.6
1983, Coalinga	P0346	6.4	29.9
1983, Coalinga	P0348	6.4	28.1
1983, Coalinga	P0353	6.4	38.8
1983, Coalinga	P0358	6.4	31.8
1983, Coalinga	P0370	6.4	27.7
1979, Imperial Valley	P0165	6.5	26.5
1979, Imperial Valley	P0166	6.5	28.7
1979, Imperial Valley	P0168	6.5	32.6
1979, Imperial Valley	P0191	6.5	26.0
1984, Morgan Hill	P0469	6.2	28.3
1986, N. Palm Springs	P0538	6.0	25.8
1987, Superstitn Hills	P0719	6.3	24.7
1987, Whittier Narrows	P0592	6.0	25.2
1987, Whittier Narrows	P0608	6.0	23.7
1987, Whittier Narrows	P0614	6.0	24.5
1987, Whittier Narrows	P0651	6.0	20.9
1987, Whittier Narrows	P0670	6.0	39.8
1987, Whittier Narrows	P0696	6.0	32.6

Table A.6: List of earthquake records used for ten-minute FAST simulations for the earthquake bin M2R3.

Earthquake	PEER Record Number	Moment Magnitude	Distance from Fault Rupture
1986, Chalfant Valley	P0549	6.2	44.9
1983, Coalinga	P0324	6.4	41.6
1983, Coalinga	P0329	6.4	46.0
1983, Coalinga	P0330	6.4	44.7
1983, Coalinga	P0331	6.4	47.3
1983, Coalinga	P0332	6.4	49.0
1983, Coalinga	P0354	6.4	41.0
1983, Coalinga	P0355	6.4	43.7
1983, Coalinga	P0356	6.4	48.0
1983, Coalinga	P0367	6.4	41.0
1979, Imperial Valley	P0167	6.5	49.3
1979, Imperial Valley	P0192	6.5	54.1
1984, Morgan Hill	P0459	6.2	54.1
1984, Morgan Hill	P0477	6.2	44.1
1986, N. Palm Springs	P0512	6.0	43.3
1986, N. Palm Springs	P0515	6.0	55.4
1986, N. Palm Springs	P0517	6.0	57.4
1986, N. Palm Springs	P0532	6.0	71.9
1986, N. Palm Springs	P0540	6.0	73.2
1986, N. Palm Springs	P0542	6.0	57.6
1987, Whittier Narrows	P0610	6.0	47.4
1987, Whittier Narrows	P0619	6.0	56.8
1987, Whittier Narrows	P0626	6.0	69.7
1987, Whittier Narrows	P0669	6.0	57.1
1987, Whittier Narrows	P0699	6.0	47.7

## Bibliography

- [1] P. Agarwal. *Structural Reliability of Offshore Wind Turbines*. PhD thesis, 2008, The University of Texas at Austin.
- [2] P. Agarwal and L. Manuel. Simulation of Offshore Wind Turbine Response for Extreme Limit States. In *Proceedings of the 26th International Conference on Offshore Mechanics and Arctic Engineering (OMAE)*, Paper No. OMAE-2007-29326, San Diego, California, 2007.
- [3] American Petroleum Institute, Washington D.C. *Recommended Practice for Design and Construction of Fixed Offshore Platforms, PR 2A, chapter 2.3.6: Earthquake.*, 2000.
- [4] N. Bazeos, G. Hatzigeorgiou, I. Hondros, H. Karamaneas, D. Karabalis, and D. Beskos. Static, seismic and stability analyses of a prototype wind turbine steel tower. *Engineering Structures*, 24(8):1015–1025, 2002.
- [5] D. Branum, S. Harmsen, S. Kalkan, M. Petersen, and C. Wills. Earthquake Shaking Potential for California. Technical Report Mapsheet 48 (Revised 2008), Department of Conservation, California Geological Survey, Sacramento, California – 95814, 2008.
- [6] C. A. Cornell. Engineering seismic risk analysis. *Bulletin of the Seismological Society of America*, 58(5):1583–1606, 1968.
- [7] Germanischer Lloyd, Hamburg, Germany. *Guideline for the Certification of Wind Turbines.*, 2003.

- [8] M. Haenler, U. Ritschel, and I. Warnke. Systematic modeling of wind turbine dynamics and earthquake loads on wind turbines. In *European Wind Energy Conference Exhibition, Athens, Greece, 2006*.
- [9] M. H. Hansen, K. Thomsen, P. Fuglsang, and T. Knudsen. Two methods for estimating aeroelastic damping for operational wind turbine modes from experiments. *Wind Energy*, 9(1-2):179–191, 2006.
- [10] International Electrotechnical Commission, Geneva, Switzerland. *IEC 61400-1 Ed. 3: Wind turbines – Part 1: Design requirements.*, 2005.
- [11] J. Jonkman, S. Butterfield, W. Musial, and G. Scott. Definition of a 5-MW Reference Wind Turbine for Offshore System Development. Technical Report NREL/TP-500-38060, National Renewable Energy Laboratory, Golden, Colorado – 80401, February 2009.
- [12] J. B. Jonkman and M. L. Buhl Jr. Turbsim User’s Guide. Technical Report NREL/TP-500-41136, National Renewable Energy Laboratory, Golden, Colorado – 80401, February 2007.
- [13] J. M. Jonkman. Dynamics Modeling and Loads Analysis of an Offshore Floating Wind Turbine. Technical Report NREL/TP-500-41958, National Renewable Energy Laboratory, Golden, Colorado – 80401, November 2007.
- [14] J. M. Jonkman and M. L. Buhl Jr. Fast User’s Guide. Technical Report NREL/EL-500-38230, National Renewable Energy Laboratory, Golden, Colorado – 80401, August 2005.

- [15] I. Lavassas, G. Nikolaidis, P. Zervas, E. Efthimiou, I. Doudomis, and C. Baniotopoulos. Analysis and design of the prototype of a steel 1-MW wind turbine tower. *Engineering Structures*, 25(8):1097–1106, 2003.
- [16] I. Prowell, A. Elgamal, and J. Jonkman. FAST Simulation of Wind Turbine Seismic Response. In *Asian–Pacific Network of Centers for Earthquake Engineering Research (ANCER) Workshop, Urbana–Champaign, Illinois*, August, 2009.
- [17] I. Prowell, A. Elgamal, H. Romanowitz, J. E. Duggan, and J. Jonkman. Earthquake Response Modeling for a Parked and Operating Megawatt-scale Wind Turbine. Technical Report NREL/TP–5000–48242, National Renewable Energy Laboratory, Golden, Colorado – 80401, October 2010.
- [18] I. Prowell, A. Elgamal, C. Uang, and J. Jonkman. Estimation of Seismic Load Demand for a Wind Turbine in the Time Domain. In *European Wind Energy Conference, Warsaw, Poland*, 2010.
- [19] I. Prowell and P. Veers. Assessment of Wind Turbine Seismic Risk: Existing Literature and Simple Study of Tower Moment Demand. Technical Report SAND2009–1100, Sandia National Laboratories, Albuquerque, New Mexico – 95814, March 2009.
- [20] U. Ritschel, I. Warnke, J. Kirchner, and B. Meussen. Wind turbines and earthquakes. In *World Wind Energy Conference, Cape Town, South Africa*, 2003.
- [21] V. A. Riziotis, S. G. Voutsinas, E. S. Politis, and P. K. Chaviaropoulos. Aeroelastic stability of wind turbines: the problem, the methods and the issues. *Wind Energy*, 7(4):373–392, 2004.

- [22] Wind Energy Department of Risø National Laboratory and Det Norske Veritas, Copenhagen, Denmark. *Guidelines for Design of Wind Turbines.*, 2001.
- [23] D. Witcher. Seismic analysis of wind turbines in the time domain. *Wind Energy*, 7(4):81–91, 2005.
- [24] P. Zhang, Z. Yang, H. Gupta, S. C. Bhatia, and K. M. Shedlock. Global seismic hazard assessment program (GSHAP) in continental Asia. *Annali Di Geofisica*, 42(6):1167–1190, 1999.
- [25] X. Zhao and P. Maisser. Seismic response analysis of wind turbine towers including soil–structure interaction. *Proceedings of the Institution of Mechanical Engineers, Part K: Journal of Multi-body Dynamics*, 220(1):53–61, 2006.
- [26] X. Zhao, P. Maisser, and W. Jingyan. A new multibody modeling methodology for wind turbine structures using a cardanic joint beam element. *Renewable Energy*, 32(3):532–546, 2007.

## Vita

Himanshu Arora was born in New Delhi, India on July 26th, 1987, the son of Sri. Suresh Arora and Smt. Vijay Arora. He graduated from Hans Raj Model School in 2005. He studied Civil Engineering at the Indian Institute of Technology Kanpur where he received his Bachelor of Technology degree in 2009. He applied to the Department of Civil, Architectural, and Environmental Engineering at the University of Texas at Austin for enrollment in their structural engineering program. He was accepted and started graduate studies in August, 2009.

Permanent address: House # 896  
Sector - 40, Gurgaon  
Haryana - 122001  
India

This thesis was typeset with L<sup>A</sup>T<sub>E</sub>X<sup>†</sup> by the author.

---

<sup>†</sup>L<sup>A</sup>T<sub>E</sub>X is a document preparation system developed by Leslie Lamport as a special version of Donald Knuth's T<sub>E</sub>X Program.